

# The morphology of galactic rings exterior to evolving bars: test-particle simulations

Micaela Bagley,<sup>★</sup> Ivan Minchev and Alice C. Quillen

*Department of Physics and Astronomy, University of Rochester, Rochester, NY 14627, USA*

Accepted 2009 January 27. Received 2009 January 27; in original form 2008 August 7

## ABSTRACT

The morphology of the outer rings of early-type spiral galaxies is compared to integrations of massless collisionless particles initially in nearly circular orbits. Particles are perturbed by a quadrupolar gravitational potential corresponding to a growing and secularly evolving bar. We find that outer rings with R1R2 morphology and pseudo-rings are exhibited by the simulations even though they lack gaseous dissipation. Simulations with stronger bars form pseudo-rings earlier and more quickly than those with weaker bars. We find that the R1 ring, perpendicular to the bar, is fragile and dissolves after a few bar rotation periods if the bar pattern speed increases by more than  $\sim 8$  per cent, bar strength increases (by  $\gtrsim 140$  per cent) after bar growth or the bar is too strong ( $Q_T > 0.3$ ). If the bar slows down after formation, pseudo-ring morphology persists and the R2 ring perpendicular to the bar is populated due to resonance capture. The R2 ring remains misaligned with the bar and increases in ellipticity as the bar slows down. The R2 ring becomes scalloped and does not resemble any ringed galaxies if the bar slows down more than 3.5 per cent suggesting that bars decrease in strength before they slow down this much. We compare the morphology of our simulations to *B*-band images of nine ringed galaxies from the Ohio State University Bright Spiral Galaxy Survey, and we find a reasonable match in morphologies to R1R2' pseudo-rings seen within a few bar rotation periods of bar formation. Some of the features previously interpreted in terms of dissipative models may be due to transient structure associated with recent bar growth and evolution.

**Key words:** galaxies: evolution – galaxies: spiral.

## 1 INTRODUCTION

Rings in barred galaxies can exist interior to the bar, encircling the bar or exterior to the bar. For a review on classification and properties of ringed galaxies, see Buta & Combes (1996). The outer rings of barred galaxies are classified as R1 or R2 depending upon whether the ring is oriented with major axis perpendicular to the bar (R1) or parallel to it (R2) (e.g. Romero-Gomez et al. 2006). If the ring is broken, partial or is a tightly wrapped spiral, it is called a pseudo-ring and denoted R1' or R2'. Some galaxies contain both types of rings and are denoted as R1R2' or R1R2. R1' and R2' morphologies were predicted as morphological patterns that would be expected near the outer Lindblad resonance (OLR) with the bar (Schwarz 1981, 1984). Rings are often the site of active star formation and so are prominent in blue visible band images,  $H\alpha$  narrow band images, and H I emission (Buta & Combes 1996).

Orbital resonances, denoted as Lindblad Resonances, occur at locations in the disc where

$$\Omega_b = \Omega \pm \kappa/m, \quad (1)$$

where  $\Omega_b$  is the angular rotation rate of the bar pattern and  $m$  is an integer. Here,  $\Omega(r)$  is the angular rotation rate of a star in a circular orbit at radius  $r$  and  $\kappa(r)$  is the epicyclic frequency. The  $m = 2$  OLR is that with  $\Omega_b = \Omega + \kappa/2$ . Orbits of stars are often classified in terms of nearby periodic orbits that are closed in the frame rotating with the bar. Near resonances, orbits become more elongated and have higher epicyclic amplitudes. Exterior to the OLR, periodic orbits parallel to the bar are present whereas interior to the OLR both perpendicular and parallel periodic orbits are present. For a steady pattern, closed orbits interior to the OLR are expected to be aligned with major axis perpendicular to the bar whereas those exterior to the OLR are aligned parallel to it (e.g. Contopoulos & Grosbøl 1989; Kalnajs 1991).

A common assumption is that rings form because gas accumulates at resonances. This follows as gas clouds cannot follow self-intersecting orbits without colliding. Because of dissipation in the gas, the bar can exert a net torque on the gas leading to a transfer

<sup>★</sup>E-mail: micaela.bagley@rochester.edu

of angular momentum. The torque is expected to change sign at resonances so gas can move away from them or accumulate at them. The corotation radius (CR) region is expected to be depopulated leading to gas concentrations at the OLR and inner Lindblad resonance (ILR) resonances. Gaseous rings form when gas collects into the largest periodic orbit near a resonance that does not cross another periodic orbit (Schwarz 1984).

Schwarz (1981, 1984) first demonstrated the efficiency of this process. Other papers have confirmed and extended this work (e.g. Combes & Gerin 1985; Byrd et al. 1994; Salo et al. 1999; Rautiainen & Salo 2000; Rautiainen, Salo & Buta 2004). Because dissipation is thought to be important, spiral-like features and ovals that are not perfectly aligned with the bar, similar to those observed, are predicted. In some cases galaxy morphology and kinematics have not been successfully modelled with a single steady-state bar component. Improvements in the models have been made with the addition of an additional exterior oval or spiral component (e.g. Hunter et al. 1988; Lindblad, Lindblad & Athanassoula 1996).

Previous work accounting for ring galaxy morphology has primarily simulated the gas dynamics using sticky-particle simulations that incorporate dissipative or inelastic collisions. Rautiainen & Salo (2000) ran  $N$ -body stellar simulations coupled with sticky gas particles. These simulations have self-consistent bars so that the orbits of the stars in the bars are consistent with the bar's gravitational potential. The disadvantage of using  $N$ -body simulations is that the properties of the bar such as its pattern speed and strength cannot be set. They can only be changed indirectly by varying the initial conditions of the simulations. An alternative approach is to set the bar perturbation strength, shape and pattern speed and search for likely bar parameters consistent with the properties of observed galaxies (e.g. Salo et al. 1999; Rautiainen et al. 2004; Rautiainen, Salo & Laurikainen 2008).

Previous work has explored the effect of bar strength and pattern speed on ring morphology (e.g. Salo et al. 1999; Rautiainen et al. 2004, 2008) and length of time since the bar grew (e.g. Ann & Lee 2000; Rautiainen & Salo 2000). Here, we explore the role of bar evolution on ring galaxy morphology. By bar evolution we mean changes in bar pattern speed and strength during and after bar growth.  $N$ -body simulations lacking live haloes predict long-lived bars with nearly constant pattern speeds (e.g. Voglis, Harsoula & Contopoulos 2007). However angular momentum transfer between a bar and the gas disc either interior or exterior to the bar or between a bar and a live halo can cause the pattern speed to vary (e.g. Debattista & Sellwood 1998; Bournaud & Combes 2002; Athanassoula 2003; Das et al. 2003; Martinez-Valpuesta, Shlosman & Heller 2006; Sellwood & Debattista 2006). Thus, constraints on the secular evolution of bars could tell us about the coupling between bars, gas and dark haloes.

Gas and stars exterior to a bar are sufficiently distant and moving sufficiently slowly compared to the bar that they are unlikely to cause strong perturbations in the orbits of stars in the bar. Because a calculation of the gravitational potential involves a convolution with an inverse square law function, high-order Fourier components are felt only extremely weakly exterior to the bar. The dominant potential term exterior to the bar is the quadrupolar term which decreases with radius to the third power,  $\Phi \propto r^{-3}$ .

Here, we explore the role of a changing quadrupolar potential field on the morphology of stars exterior to a bar. In this work, we focus on collisionless stellar orbits and leave investigating the study of dissipative effects for future study. In Section 2, we describe our simulations and present the results obtained by varying the parameters. In Section 3, we compare the results of our simulations with

nine galaxies from the Ohio State University Bright Spiral Galaxy Survey (OSUBSGS; Eskridge et al. 2000). Finally, in Section 4 we summarize and discuss our results.

## 2 TEST-PARTICLE SIMULATIONS

We perform 2D test-particle simulations of an initially axisymmetric galactic disc that is perturbed by a forcing bar pattern. The rotation curve adopted for a particle in a circular orbit is

$$v_c(r) = s^{\gamma/2} \quad (2)$$

with  $s = \sqrt{r^2 + a^2}$  and  $a > 0$  a core radius to prevent extreme orbits near the galaxy centre. A flat rotation curve has  $\gamma = 0$ . This curve corresponds to an axisymmetric potential

$$\Phi_0(s) = \begin{cases} \log(s) & \text{for } \gamma = 0 \\ \gamma^{-1}s^\gamma & \text{for } \gamma \neq 0. \end{cases} \quad (3)$$

To this axisymmetric component, we add a quadrupole perturbation for the bar in the form used by Dehnen (2000) and Minchev, Nordhaus & Quillen (2007),

$$\Phi_b(r, \phi, t) = \epsilon \cos[2(\phi - \Omega_b t)] \times \begin{cases} (r_b/r)^3, & r > r_b, \\ 2 - (r/r_b)^3, & r \leq r_b, \end{cases} \quad (4)$$

where  $r_b$  is the bar length and  $\Omega_b$  its angular rotation rate or pattern speed.

As we wish to explore bars with changing pattern speeds, we allow  $\Omega_b$  to vary with time; however, we fix the ratio of the CR to the bar length, ( $R$ ), so that

$$r_b(t) = r_{b,0} \frac{\Omega_{b,0}}{\Omega_b(t)}. \quad (5)$$

Previous studies have found that bars end interior to their CR,  $r_{CR}$ , with the ratio of bar CR to bar length ( $R$ ) = 1.1–1.43 (Athanassoula 1992; Rautiainen et al. 2008). We describe pattern speed variations with two parameters: the rate of change during bar growth,  $d\Omega_g/dt$ , and that after bar growth,  $d\Omega_b/dt$ . The bar strength grows linearly with time,  $\epsilon \propto t$ , until a time  $t_{\text{grow}}$ , at which time it reaches a strength  $\epsilon_{\text{lgrow}}$ . After  $t_{\text{grow}}$ , the bar strength may vary at a slower rate,  $d\epsilon/dt$ .

Previous work has used as a measure of bar strength the parameter  $Q_T$  (Combes & Sanders 1981). At a given radius, this is the ratio of the maximum tangential force to the azimuthally averaged radial force. Here, equation (4) implies that  $Q_T$  near the end of the bar is  $Q_T = 2\epsilon$ .

Fig. 1 shows the ratio  $Q_T(r)$  as a function of radius or the maximum tangential to azimuthally averaged radial force as a function of radius. Assumed is a flat rotation curve and potential given in equations (1)–(3). Unlike that of Laurikainen et al. (2004, see their fig. 8), our  $Q_T$  profile has a maximum at  $r_b = 0$ .  $Q_T$  decays more slowly past the end of the bar than it increases inside the bar radius.

The solid curves in Fig. 1 are for different values of bar strength  $|\epsilon|$ , with the thickest corresponding to the parameters of simulation 1:  $|\epsilon| = 0.10$  and  $r_b/r_{b,0} = 1.0$ . The remaining two solid curves illustrate the range in strengths used in simulations 25–34, in which the bar strength is varying after bar growth. The dotted curves show the range of bar lengths used in simulations 2–19.  $r_b = 1.07$  corresponds to the minimum pattern speed resulting when the pattern speed decreases after bar growth (simulation 11) while  $r_b = 0.91$  corresponds to the maximum pattern speed resulting when the pattern speed increases after bar growth (simulation 6).  $r_b = 1.43$  corresponds to the minimum pattern speed resulting when the pattern speed decreases during bar growth (simulation 19) while

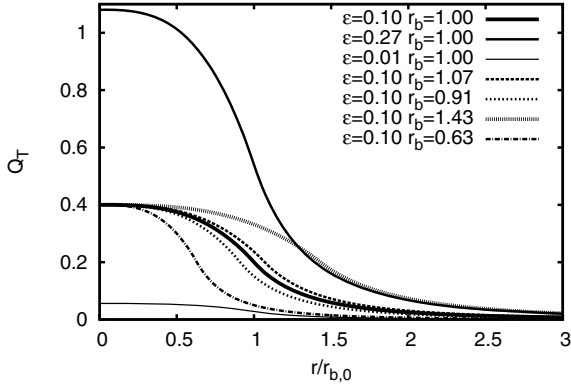


**Figure 1.** Shown is the ratio  $Q_T(r)$  as a function of radius or the maximum tangential to azimuthally averaged radial force as a function of radius. Assumed is a flat rotation curve and potential given in equations (1)–(3). The solid curves are for different values of bar strength  $|\epsilon|$  and illustrate the range of strengths used in simulations 25–34 with varying bar strength (maximum  $|\epsilon|$  is for simulation 29 and minimum for simulation 34). The dotted curves show the range of bar lengths which correspond to simulations 2–19 that have bars that have sped up or slowed down. (Maximum  $r_b = 1.07$  corresponds to simulation 11 and minimum  $r_b = 0.91$  to simulation 6, with bar pattern speed decreasing and increasing, respectively, after bar growth. Maximum  $r_b = 1.43$  corresponds to simulation 19 and minimum  $r_b = 0.63$  corresponds to simulation 15, with bar pattern speed decreasing and increasing, respectively, during bar growth.)

$r_b = 0.63$  corresponds to the maximum pattern speed resulting when the pattern speed increases during bar growth (simulation 15).

Changes in bar pattern speed subsequently change the locations of the corotation and OLR radii. This change is shown wherever applicable in our simulation with solid circles plotted at the locations of the bar’s corotation and 2:1 OLR. For the maximum pattern speed change after bar growth of simulation 6, the CR and the OLR move inwards by 9.1 per cent. The locations of the radii move inwards 37 per cent in simulation 15, which has a maximum pattern speed from a bar that speeds up during bar growth. The locations of the radii move outwards by 6.67 and 42.9 per cent for simulations 11 (pattern speed decreasing after bar growth) and 19 (during bar growth), respectively.

The simulations presented here integrate  $10^5$  particles with a fourth-order Runge–Kutta method. All particles are integrated simultaneously in parallel on a NVIDIA GeForce 8800 GTX graphics card. The code is written with NVIDIA’s Compute Unified Device Architecture (CUDA), the C-language development environment for CUDA-enabled Graphics Processing Units (GPUs).

Particle initial conditions are nearly circular orbits with epicyclic amplitude randomly generated so the initial velocity dispersion is  $\sigma$  times the circular velocity. In our simulations, the velocity dispersion is about 0.04 of the circular velocity, which is about  $7 \text{ km s}^{-1}$  for a galaxy with a  $200 \text{ km s}^{-1}$  rotational velocity. For comparison, H I linewidths are typically in the range of  $5\text{--}10 \text{ km s}^{-1}$ . The epicyclic amplitude distribution is Gaussian. Initial radii are chosen from a flat distribution with minimum and maximum radius between 0.5 and 4.0 times the initial bar length. This leads to an initial disc surface density proportional to  $1/r$ .

Unless otherwise noted, when we discuss times in terms of bar periods we are referring to the initial bar period, which has time  $P_{b,0} = 2\pi/\Omega_{b,0}$ . We run our simulations for 25 bar periods, and the bar grows for the first 3 bar rotation periods;  $t_{\text{grow}} = 3$ . We focus on a ratio of bar CR to bar length of  $(R) = 1.25$ , so that the initial bar pattern speed is  $\Omega_{b,0} = 0.8$  and the CR is therefore  $r_{\text{CR}} = 1.25$ . Table 1 lists the initial conditions that all of our simulations have in common. Table 2 lists remaining simulation parameters. The majority of our simulations have bars of strength  $|\epsilon_{\text{igrow}}| = 0.10$ , corresponding to  $Q_T = 0.2$ . Lengths are given in terms of the initial bar length,  $r_{b,0}$ , and angular velocities are given in terms of that at a radius of the initial bar length. We use negative values of  $\epsilon$  to signify that initially  $\phi = 0$  corresponds to the bar major axis.

## 2.1 Description of simulations

Snapshots at different times for simulation 1 with parameters listed in Tables 1 and 2 are shown in Figs 2 and 3. Simulation 1 is our base or comparison simulation, with  $|\epsilon_{\text{igrow}}| = 0.10$ , corresponding to  $Q_T = 0.2$ , and bar grown in  $t_{\text{grow}} = 3$  bar rotation periods. In Figs 2 and 3, each frame has been rotated so that the bar is horizontal. Fig. 2 shows the first 4 bar periods simulation 1 with each image separated in time by a quarter bar period to emphasize the structure evident during bar growth. The bar is growing up to the left-hand side image of the bottom row. Fig. 3 shows snapshots of the 25 bar periods of the simulation with each image separated by 2.5 bar periods, so that the first image is shown at a time 2.5 bar periods into bar growth. The solid circles in the first image of each figure are plotted at the bar’s corotation resonance and 2:1 OLR. As can be seen from Fig. 2, during bar growth, strong open spiral-like structure is present that might be interpreted as an R1’ ring. Just after bar growth (see Fig. 3), both R1 and R2 rings are present but the R2 ring is not always oriented parallel to the bar. For up to 5 bar rotation periods following bar growth, there are azimuthal variations in density in the rings as well as shifts in the R2 ring orientation so they could be considered pseudo-rings. After bar growth, the structure

**Table 1.** Common parameters for simulations.

	Parameter	Value	Comments
1	$\gamma$	0.0	Sets the slope of the rotation curve
2	$t_{\text{grow}}$	3	Bar growth time in bar rotation periods
3	$\Omega_{b,0}$	0.8	Initial bar pattern speed
4	$r_{b,0}$	1.0	Initial bar length
5	$r_{\text{CR}}$	1.25	Radius of corotation
6	$(R)$	1.25	Ratio of bar CR to bar length
7	$\sigma$	0.036	Initial velocity dispersion in units of the circular velocity

With the exception of simulations 35 and 36, these parameters are not altered from simulation to simulation. Length-scales are given in units of the initial bar length. Angular rotation rates are given in units of that at  $r_{b,0}$ . The initial bar rotation period is  $P_{b,0} = 2\pi/\Omega_{b,0}$ . For simulation 35,  $\Omega_{b,0} = 0.7$ ,  $r_{\text{CR}} = 1.43$  and  $(R) = 1.43$ . For simulation 36,  $\Omega_{b,0} = 0.9$ ,  $r_{\text{CR}} = 1.1$  and  $(R) = 1.1$ .

**Table 2.** Additional parameters for Simulations.

Sim. 1	$d\Omega_b/dt$ 2	Per cent 3	$d\Omega_g/dt$ 4	per cent 5	$ \epsilon_{\text{igrow}} $ 6	$d \epsilon /dt$ 7	Per cent 8
1	0.00	0.00	0.0	0.0	0.10	0.0	0.0
2	0.0001	2.16	0.0	0.0	0.10	0.0	0.0
3	0.0002	4.32	0.0	0.0	0.10	0.0	0.0
4	0.0003	6.48	0.0	0.0	0.10	0.0	0.0
5	0.0004	8.64	0.0	0.0	0.10	0.0	0.0
6	0.0005	10.80	0.0	0.0	0.10	0.0	0.0
7	-0.0001	-2.16	0.0	0.0	0.10	0.0	0.0
8	-0.00015	-3.24	0.0	0.0	0.10	0.0	0.0
9	-0.0002	-4.32	0.0	0.0	0.10	0.0	0.0
10	-0.00025	-5.40	0.0	0.0	0.10	0.0	0.0
11	-0.0003	-6.48	0.0	0.0	0.10	0.0	0.0
12	0.0	0.0	0.005	14.73	0.10	0.0	0.0
13	0.0	0.0	0.01	29.45	0.10	0.0	0.0
14	0.0	0.0	0.015	44.18	0.10	0.0	0.0
15	0.0	0.0	0.02	58.90	0.10	0.0	0.0
16	0.0	0.0	-0.0025	-7.36	0.10	0.0	0.0
17	0.0	0.0	-0.005	-14.73	0.10	0.0	0.0
18	0.0	0.0	-0.0075	-22.09	0.10	0.0	0.0
19	0.0	0.0	-0.01	-29.45	0.10	0.0	0.0
20	0.0	0.0	0.0	0.0	0.06	0.0	0.0
21	0.0	0.0	0.0	0.0	0.08	0.0	0.0
22	0.0	0.0	0.0	0.0	0.12	0.0	0.0
23	0.0	0.0	0.0	0.0	0.14	0.0	0.0
24	0.0	0.0	0.0	0.0	0.16	0.0	0.0
25	0.0	0.0	0.0	0.0	0.10	0.0002	34.56
26	0.0	0.0	0.0	0.0	0.10	0.0004	69.12
27	0.0	0.0	0.0	0.0	0.10	0.0006	103.7
28	0.0	0.0	0.0	0.0	0.10	0.0008	138.2
29	0.0	0.0	0.0	0.0	0.10	0.0010	172.8
30	0.0	0.0	0.0	0.0	0.10	-0.0001	-17.28
31	0.0	0.0	0.0	0.0	0.10	-0.0002	-34.56
32	0.0	0.0	0.0	0.0	0.10	-0.0003	-51.84
33	0.0	0.0	0.0	0.0	0.10	-0.0004	-69.12
34	0.0	0.0	0.0	0.0	0.10	-0.0005	-86.39
35	0.0	0.0	0.0	0.0	0.10	0.0	0.0
36	0.0	0.0	0.0	0.0	0.10	0.0	0.0

Length-scales are given in units of the initial bar length. Velocities are given in units of the circular velocity at the initial bar end. Time is given in units such that the period of rotation is  $2\pi$  at  $r_{b,0}$ . Angular rotation rates are in units of that at  $r_{b,0}$ . The initial bar period is  $P_{b,0} = 2\pi/\Omega_{b,0}$ . Bar strength is given in units of the square of the circular velocity at  $r_{b,0}$ . Column (1): simulation. Column (2):  $d\Omega_b/dt$  is the rate of bar pattern speed change after bar growth. Column (3): the per cent by which the bar pattern speed has changed by  $t = 25 P_{b,0}$ , after 25 bar rotation periods. Column (4):  $d\Omega_g/dt$  is the rate of bar pattern speed change during bar growth. Column (5): the per cent by which the bar pattern speed has changed by the end of bar growth. Column (6):  $\epsilon_{\text{igrow}}$  is the bar strength at the end of bar growth or at time  $t = t_{\text{grow}}$ . Column (7):  $d|\epsilon|/dt$  is the bar strength rate of change after  $t_{\text{grow}}$ . Column (8): the per cent by which the bar strength changes by  $t = 25 P_{b,0}$ . *Note.* simulations 35 and 36 have initial bar pattern speeds of  $\Omega_{b,0} = 0.7$  and  $0.9$ , respectively, whereas all other simulations have  $\Omega_{b,0} = 0.8$  (see Table 1).

stabilizes and R1 and R2 rings remain that are increasingly mirror symmetric and remain oriented perpendicular and parallel to the bar, respectively.

The bar is grown sufficiently slowly that the orbits change adiabatically. Orbits remain near to closed or periodic orbits, and structure associated with both R1 and R2 orbit families is seen. Most interesting is that the simulation displays twists in the density peaks, azimuthal variations in the density of the ring and deviations of ring orientation from perpendicular and parallel to the bar at the end of and a few periods after bar growth. Previous work has suggested that weak dissipation is required to exhibit spiral structure or pseudo-ring morphology; however, here we see transient spiral structures induced by bar growth and pseudo-ring type morphology for a few

rotation periods following bar growth. After  $\sim 5$  periods, the asymmetries are reduced and the morphology contains both stable R1- and R2-type rings.

Our simulation looks similar to the sticky-particle simulations by Schwarz (1981) and Byrd et al. (1994). Their simulations also displayed early spiral structure. The sticky-particle simulations exhibit strong R1' morphology for a few bar rotation periods. Our simulation exhibits R1'-type morphology only during bar growth, R1R2' morphology a few rotation periods after bar growth and stable R1R2 morphology on long time-scales.

During bar growth, these simulations look remarkably similar to the sticky-particle simulations by Rautiainen et al. (2004, 2008) even though they lack dissipation. *N*-body and smoothed particle

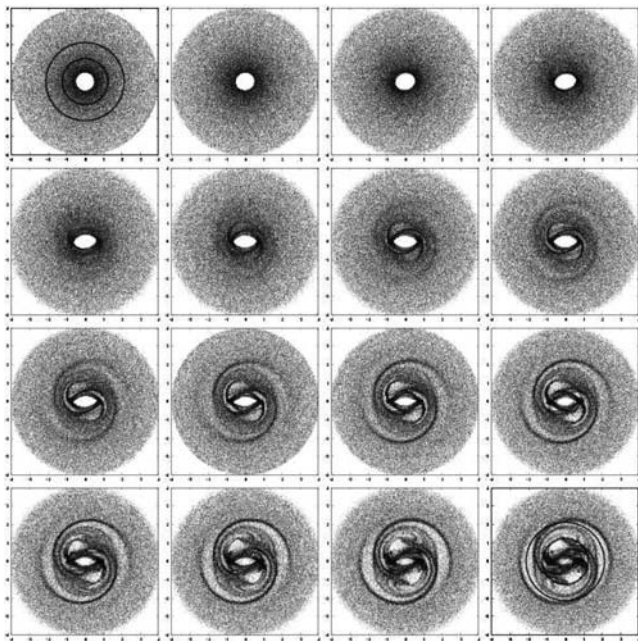


**Figure 2.** Bar growth in simulation 1. The distribution of collisionless particles is shown every quarter bar period. The bar is growing up to the left-hand side image of the last row. Solid circles are shown at the location of the bar's corotation resonance and 2:1 OLR at the beginning of the simulation. Strong open spiral-like structure is evident during bar growth even though the simulation is lacking gaseous dissipation.

hydrodynamic (SPH) simulations often suffer from artificially heating. Fine structure that would only be present in a perturbed initially cold population might not survive due to excess heating inherent in the simulation. Sticky particle and SPH simulations, because they allow dissipation, can reduce the velocity dispersion of the particles. The similarity between the sticky-particle simulations and the dissipationless simulations shown here could be because our initial orbits were nearly circular.

The ability of collisionless simulations to display R1R2-type morphology suggests that we reexamine the role of dissipation in influencing ring galaxy morphology. SPH simulations (Ann & Lee 2000; Bissantz, Englmaier & Gerhard 2003) sometimes show open outer spiral arms that are similar to R1' pseudo-rings and resemble morphology during bar growth seen here. Our simulations stop showing spiral structure soon after bar growth. Hänninen & Salo (1992) show that there is a close correspondence between simulations with dissipation and those without during the initial transient stage, but that spiral structure then disappears for dissipationless simulations. The SPH simulations by Ann & Lee (2000) show R1'-type pseudo-ring morphology but only within a few rotation periods after bar growth. Likewise, the sticky-particle simulations by Rautiainen & Salo (2000) show R1 or R2 or both R1R2 ring morphology, but only within a few bar rotation periods after bar growth (see their fig. 10). The SPH simulations by Ann & Lee (2000) show spiral structure for a somewhat longer time than ours (a few bar rotations following bar growth), but they fail to exhibit R1 or R2 ring morphology.

We find that R1R2 rings (systems with both types of features) do not require dissipation for formation; however, they do require particles to be on nearly closed orbits. This can result either because of dissipation or because gas and recently born stars tend to be on nearly circular orbits prior to bar growth. The success of sticky-

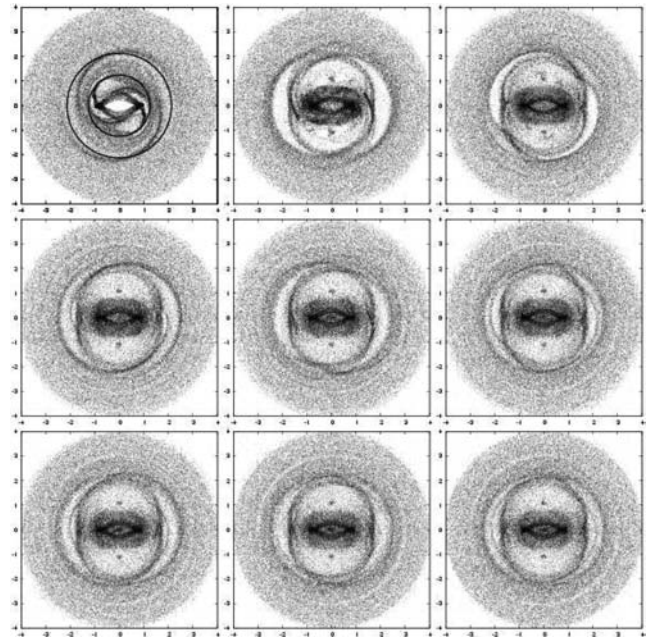


**Figure 3.** Simulation 1, with bar angular rotation rate  $\Omega_{b,0} = 0.8(R = 1.25)$ , bar strength  $|\epsilon_{t\text{grow}}| = 0.10$  (corresponding to  $Q_T = 0.2$ ) and bar grown in  $t_{\text{grow}} = 3$  bar periods. The distribution of collisionless particles is shown each 2.5 bar rotation periods, beginning 2.5 bar periods into bar growth. Therefore, the bar has almost finished growing in the first image. In the first image, solid circles are shown at the location of the bar's corotation resonance and 2:1 OLR. We note that the R2 ring is misaligned with the bar and azimuthal variations in densities are seen until  $\sim t = 5$  bar rotation periods after bar formation. Pseudo-ring morphology is present at the end of and a few rotation periods after bar growth. Both R1 and R2 rings are present and stable after bar growth. We find that collisionless particles that are initially in nearly circular orbits can display R1R2 outer ring morphology.

particle simulations in reproducing outer ring morphology may be in part because of their ability to cool or reduce the velocity dispersion of their particles. SPH simulations (e.g. Ann & Lee 2000; Bissantz et al. 2003) exhibit only R1' pseudo-ring morphology suggesting that when dissipation is large, both types of rings are not formed. Here, we see that R1R2 morphology can be long lived, though it is possible that R1R2 ring morphology is a short-lived phenomenon as many barred galaxies do not exhibit R1- or R2-type outer rings.

## 2.2 Morphology sensitivity to pattern speed variation after bar growth

We first explore the sensitivity of outer ring morphology to weak changes in bar pattern speed following bar growth. Simulations 2–6 are identical to simulation 1 except the bar pattern speed increases after bar growth. Simulations 7–11 are identical to simulation 1 except the bar pattern speed decreases after bar growth. Fig. 4 shows simulation 5, which has an increasing bar pattern speed,  $d\Omega_b/dt = 0.0004$ . For this simulation, the pattern speed increases 0.39 per cent each bar period. We have plotted solid circles on the first and last images to show how the bar's corotation and 2:1 OLRs change with the increasing bar pattern speed. We find that the R1 outer ring grows weaker as the pattern speed increases. The R1 ring has completely dissolved by the end of the simulation when the pattern speed has increased by about 9 per cent compared to its initial value. At later times, even though the perturbation is always changing, the morphology is nearly mirror symmetric. We find that spiral structure

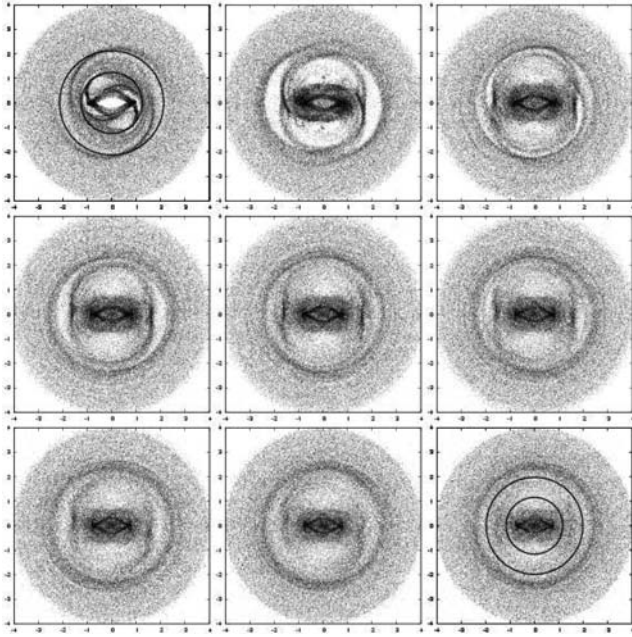


**Figure 4.** Simulation 5 showing a bar with increasing pattern speed,  $d\Omega_b/dt = 0.0004$ . The bar speeds up only after it has finished growing at 3 bar rotation periods. Each image is separated by 2.5 initial bar rotation periods. The solid circles in the first and last images show the locations of the bar's corotation resonance and 2:1 OLR. Note the loss of the R1 ring later in the simulation.

or pseudo-ring structure is not caused by the increase in bar pattern speed.

Fig. 5 shows the morphology at the end of simulations 1–6. Here, we see that the R1 ring disappears as the bar pattern speed increases. At later times in the simulations with more quickly increasing pattern speeds, the R1 ring dissolves and only a nearly circular outer

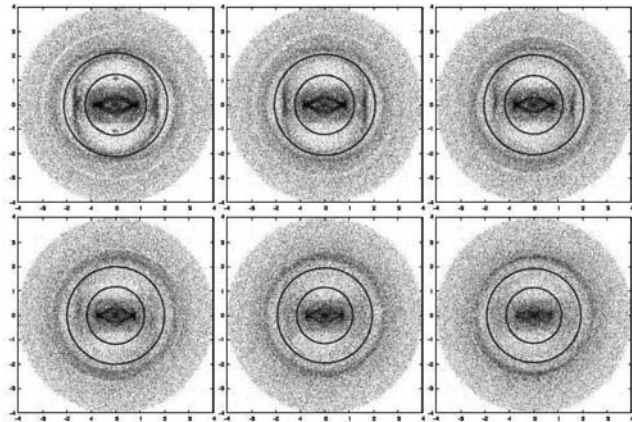


**Figure 5.** The last image of simulations 1–6. Each image shows the density distribution at a time 25 bar periods after the start of the simulation. From left- to right-hand sides: the top row shows simulation 1 with  $d\Omega_b/dt = 0.0$ ; simulation 2 with  $d\Omega_b/dt = 0.0001$  and simulation 3 with  $d\Omega_b/dt = 0.0002$ . The bottom row shows simulation 4 with  $d\Omega_b/dt = 0.0003$ , simulation 5 with  $d\Omega_b/dt = 0.0004$  and simulation 6 with  $d\Omega_b/dt = 0.0005$ . Solid circles are shown at the location of the bar's corotation resonance and 2:1 OLR and are shown in every image as the final pattern speed is different for each simulation. We find that when the bar pattern speed increases by more than  $\sim 8$  per cent the R1 ring completely dissolves.

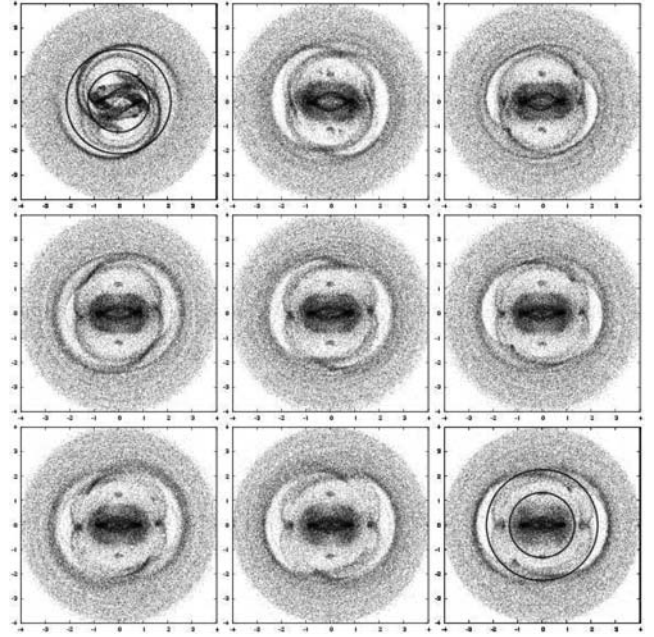


**Figure 6.** Simulation 11 showing a bar with decreasing pattern speed,  $d\Omega_b/dt = -0.0003$ . The bar slows down after it has finished growing. Each image is separated in time by 2.5 bar rotation periods. Solid circles in the first and last images show how the bar's corotation resonance and 2:1 OLR change with the decreasing bar pattern speed. We see a high epicyclic amplitude R2 ring that we attribute to resonance capture. This ring can be misaligned with the bar even at late times.

ring remains. We find that when the bar pattern speed increases by more than  $\sim 8$  per cent, the R1 ring completely dissolves.

In simulations 7–11, we decrease the bar pattern speed after bar growth. Fig. 6 shows simulation 11 with  $d\Omega_b/dt = -0.0003$ . The R2 ring in this simulation is elongated and strong and is seldom aligned parallel to the bar even at later times. While the simulation with the increasing pattern speed (shown in Fig. 4) did not exhibit pseudo-ring morphology after bar growth or misaligned R1 or R2 rings, the simulations with decreasing pattern speed do show misaligned R2-type rings even at late times. The ellipticity of the R2 ring is higher than seen in the comparison simulation shown in Fig. 3 with a bar with a constant pattern speed.

Fig. 7 shows the last periods of simulations 1 and 7–11. Here, we see that the R2 ring remains misaligned 22 bar periods after bar growth is complete when the pattern speed begins to decrease. The ellipticity of the R2 ring increases as the bar pattern speed decreases. We find that when the pattern speed decreases by more than  $\sim 3.5$  per cent, the simulations do not resemble real galaxy morphology.

Decreasing the pattern speed moves the bar's resonances outwards, as shown by the increasing radii of the solid circles in Fig. 7. Exterior to the OLR, only one family of periodic orbits exists aligned parallel to the bar. However, interior to the OLR, two families of periodic orbits exist, both those perpendicular and parallel to the bar (e.g. Contopoulos & Grosbøl 1989; Quillen 2003). When the bar slows down, orbits can be captured into resonance (e.g. Romero-Gomez et al. 2006). Only the orbit family parallel to the bar can capture particles, and as the bar pattern speed continues to decrease these orbits will increase in epicyclic amplitude. This is mathematically similar to Pluto's orbit increasing in eccentricity as Neptune migrates outwards (e.g. Quillen 2006). Resonance capture into orbits parallel with the bar is likely to explain the higher epicyclic

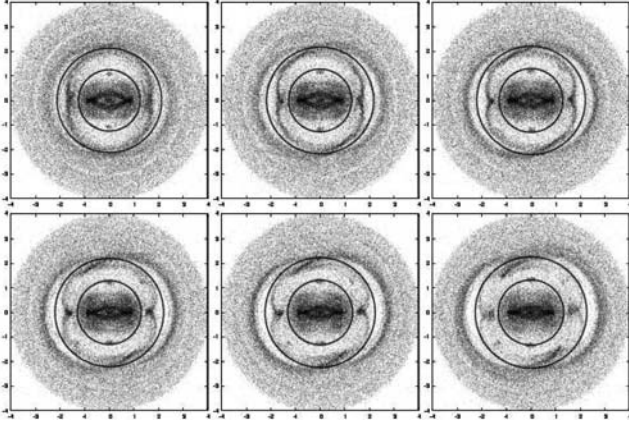


**Figure 7.** The last image of simulations 1 and 7–11. Each image shows the density distribution at a time 25 bar periods after the start of the simulation. Solid circles are shown at the location of the bars' corotation resonance and 2:1 OLR. From left- to right-hand side: the top row shows simulation 1 with  $d\Omega_b/dt = 0.0$ ; simulation 7 with  $d\Omega_b/dt = -0.0001$  and simulation 8 with  $d\Omega_b/dt = -0.00015$ . The bottom row shows simulation 9 with  $d\Omega_b/dt = -0.0002$ , simulation 10 with  $d\Omega_b/dt = -0.00025$  and simulation 11 with  $d\Omega_b/dt = -0.0003$ . We attribute the high epicyclic amplitude R2 rings to resonance capture. The R2 ring remains misaligned with the bar even 22 bar periods after the bar pattern speed began decreasing.

amplitude of the R2 rings seen in Fig. 6 in which the bar pattern is slowing down.

In summary, if the bar speeds up subsequent to bar formation (or increases in pattern speed by more than  $\sim 8$  per cent) we find that the R1 ring dissolves. Simulations with increasing pattern speeds show misaligned rings and azimuthal density contrasts only 1–2 periods after bar formation. If the bar slows down however, we find that the R2 ring is increased in strength and eccentricity and both R2 and R1 are seen even at later times ( $>20$  periods after bar formation). Furthermore, the R2 ring is misaligned with the bar for many rotation periods. If the bar pattern speed decreases by more than  $\sim 3.5$  per cent, we find that the R2 becomes unrealistically scalloped.

### 2.3 Morphology sensitivity to pattern speed variation during bar growth

We next explore the effect of altering the bar pattern speed during bar growth rather than following bar growth.  $d\Omega_g/dt$  is positive in simulations 12–15, causing the pattern speed to increase for the first 3 periods of each simulation. Fig. 8 shows simulation 13 with  $d\Omega_g/dt = 0.01$ . Open spiral arms are present at the end of the third period of bar growth. However, R1R2 double ring morphology does not form in this simulation. As was true in the simulations with bar pattern speed increasing following bar formation (simulations 2–6; see Figs 4 and 5), the R1 ring dissolves and only a nearly circular outer ring remains. We note that the spiral and outer ring structure in simulations 2–6 (see Fig. 4) did not dissolve as quickly as in simulation 13, where an R1R2 outer ring never forms. This suggests that outer ring structures are more sensitive to alterations in pattern speed during bar growth than to changes after bar growth.

Fig. 9 shows the last of the 3 periods of bar growth for simulations 1 and 12–15. The first row shows simulation 1 with  $d\Omega_g/dt = 0.0$ .  $d\Omega_g/dt$  increases by 0.005 in each consecutive simulation, corresponding to each row in Fig. 9. We note from these simulations that open spiral arms are seen during bar growth when

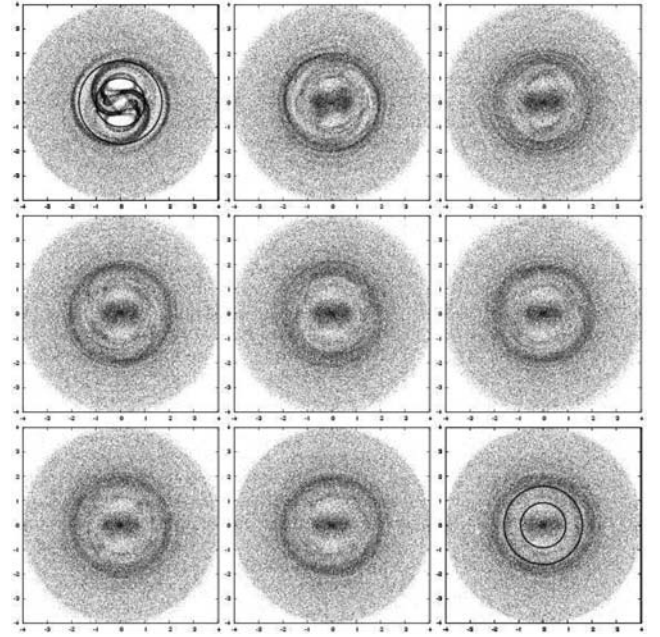


**Figure 8.** Simulation 13 showing a bar with increasing pattern speed during bar growth,  $d\Omega_g/dt = 0.01$ . The bar pattern speed is only increasing in the first image while the bar is growing. Each image is separated by 2.5 initial bar periods. Solid circles in the first and last images show how the bar's corotation resonance and 2:1 OLR change with the increasing bar pattern speed. The bar pattern speed only decreases for another 0.5 bar period following the time shown by the first image. R1R2 structure does not form as it does in Fig. 4 where the pattern speed is increasing after bar growth. Here, spiral structure dissolves within 3 periods after bar growth and only a nearly circular outer ring remains. Outer ring structures may be more sensitive to alterations in pattern speed during bar growth than to changes after bar growth.

the bar is increasing in pattern speed. The radii of spiral structure decreases as the pattern speed increases. This is expected as the radii of the resonances move inwards as the bar pattern speed increases (see the solid circles in the first and last images of each row of Fig. 9).

Fig. 5 shows that ring radial size does not decrease as the bar pattern speed increases when the pattern speed increases after bar growth. However, when the pattern speed increases during bar growth (see Fig. 9) the ring radius does decrease. This suggests that ring size is primarily set during bar growth and is not strongly affected by subsequent increases in pattern speed. Subsequent bar speed increases primarily dissolve or weaken the rings rather than change their radius.

We now compare the effect of decreasing pattern speed during bar growth with the effect of increasing pattern speed during bar growth. The pattern speed is decreasing during the 3 periods of bar growth in simulations 16–19. Fig. 10 shows snapshots from throughout simulation 17 with  $d\Omega_g/dt = -0.005$ , while (Fig. 11) shows the last of the 3 periods of bar growth for simulations 1 and 16–19. We find that when the bar pattern slows down during bar growth the outer rings are not lost as was true when the pattern speed increased during growth. The R1R2' structure seen during bar growth for simulation 1 is exhibited by simulation 17 but later, 2 to 3 periods after bar growth rather than in the first period following bar growth. During this time, the rings appear almost double or tightly wound. The pseudo-rings close, the morphology stabilizes and presents the R1R2 structure characteristic of our steady-state



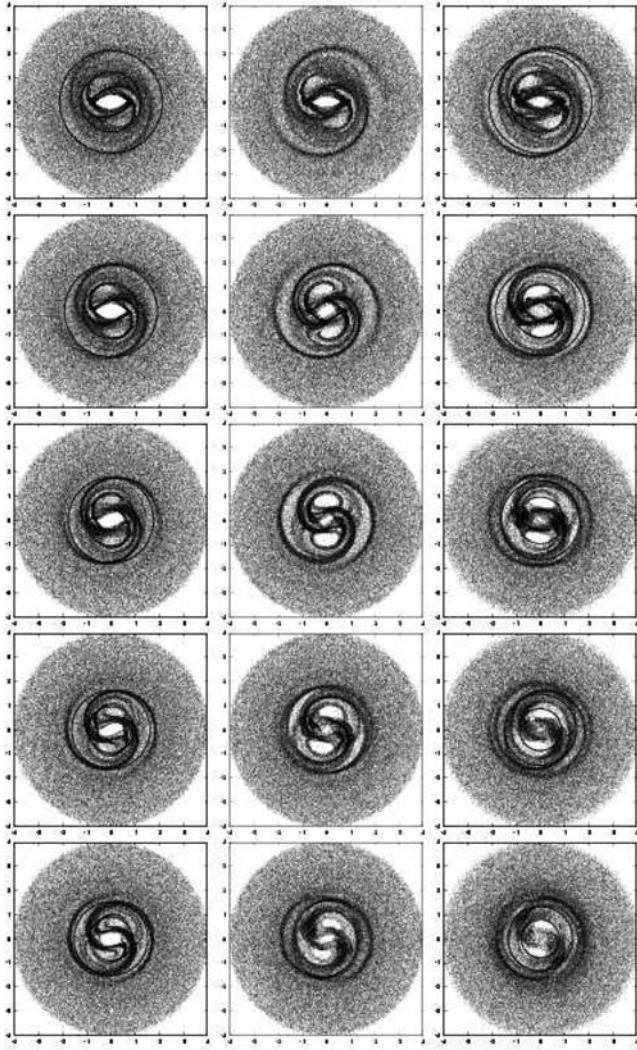


**Figure 9.** Morphology change when the pattern speed is increased during bar growth. Three images, corresponding to the last period of bar growth, of the simulations in which the pattern speed is increased during growth. From top to bottom: the rows show simulation 1 with  $d\Omega_g/dt = 0.0$ ; simulation 12 with  $d\Omega_g/dt = 0.005$ ; simulation 13 with  $d\Omega_g/dt = 0.01$ ; simulation 14 with  $d\Omega_g/dt = 0.015$  and simulation 15 with  $d\Omega_g/dt = 0.02$ . Solid circles in the first and last images of each row show how the bar's corotation resonance and 2:1 OLR change with the increasing bar pattern speed. As the pattern speed increases, the axes of the rings decrease.

comparison simulation shown in Fig. 3. As is expected from the location of the OLR (note the change in size of the solid circles in Fig. 10), the ring radii become larger if the bar pattern speed decreases.

The first row of Fig. 11 shows simulation 1 with  $d\Omega_g/dt = 0.0$ .  $d\Omega_g/dt$  decreases by 0.0025 in each consecutive simulation, corresponding to each row in Fig. 11. The decreasing pattern speed seems to delay the formation of strong spiral structure. Fig. 9 showing morphology during bar growth for a bar that is speeding up can be compared to Fig. 11 that shows morphology during bar growth for a bar that is slowing down. The simulation with the largest decrease in pattern speed shows the weakest spiral structure during bar growth and that with the largest increase in pattern speed the strongest spiral structure earliest.

In summary, we find that if the bar pattern speed is decreasing during growth, transient spiral structure is weaker during growth and

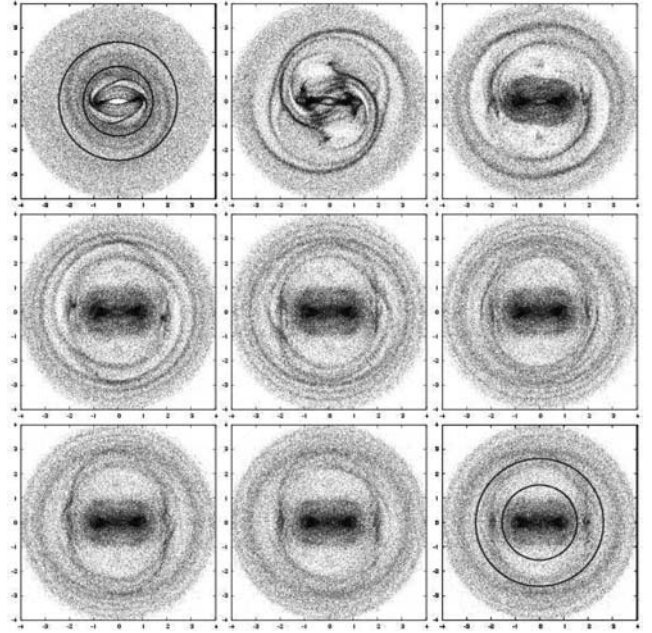


**Figure 10.** Simulation 17 with  $d\Omega_g/dt = -0.005$ . The pattern speed is decreasing during bar growth. Solid circles in the first and last images show how the bar's corotation resonance and 2:1 OLR change with the decreasing bar pattern speed. The bar pattern speed only decreases for another 0.5 bar period following the time shown by the first image. Each image is separated by 2.5 bar rotation periods. The transient spiral structure during bar growth is weaker than when bar pattern is fixed (see Fig. 2). Formation of the R1 and R2 rings is delayed in this simulation and occurs after the bar has finished growing compared to that with a fixed pattern speed.

the formation of the R1 and R2 ring structure is delayed by a few bar rotation periods. If the bar pattern speed increases during rather than after growth, the outer rings are smaller. An increase in pattern speed during bar growth destroys the R1 ring and asymmetries typical of pseudo-rings.

#### 2.4 Morphology sensitivity to bar strength

We now explore the sensitivity of the morphology to bar strength. The bar strength increases linearly with time during bar growth until, at  $t = t_{\text{grow}}$ , it reaches a strength determined by the parameter  $|\epsilon_{\text{t grow}}|$ . Thus a lower value of  $|\epsilon_{\text{t grow}}|$  results in both a weaker bar at  $t = t_{\text{grow}}$  and a slower rate of bar growth. Simulations 20 and 21 have weaker bars, lower  $|\epsilon_{\text{t grow}}|$ , than our comparison simulation shown in Fig. 3. During and right after bar growth in simulations 20 and 21, we see the open spiral structure evident in Fig. 3. In simulations 20 and 21, the R2 ring is misaligned with the bar for up to 6 bar rotation periods following bar growth, whereas the R2 ring in Fig. 3 is misaligned for 5 bar periods following bar growth. The time-scale for misalignment in the R2 ring is probably related to the bar strength, which would set the libration time-scale in the OLR. The R1 and R2 rings become increasingly mirror symmetric. They remain strong, stable and oriented perpendicular and parallel to the bar, respectively.

Simulations 22–24 have stronger bars, and the spiral structure evident during and right after bar growth is much stronger than that of Fig. 3. The R2 rings in simulations 22–24 are misaligned with the bar for only 3 to 4 bar periods following bar growth. R1 and R2 rings form earlier, and we see a weakening of the R1 ring at later times of the simulations.



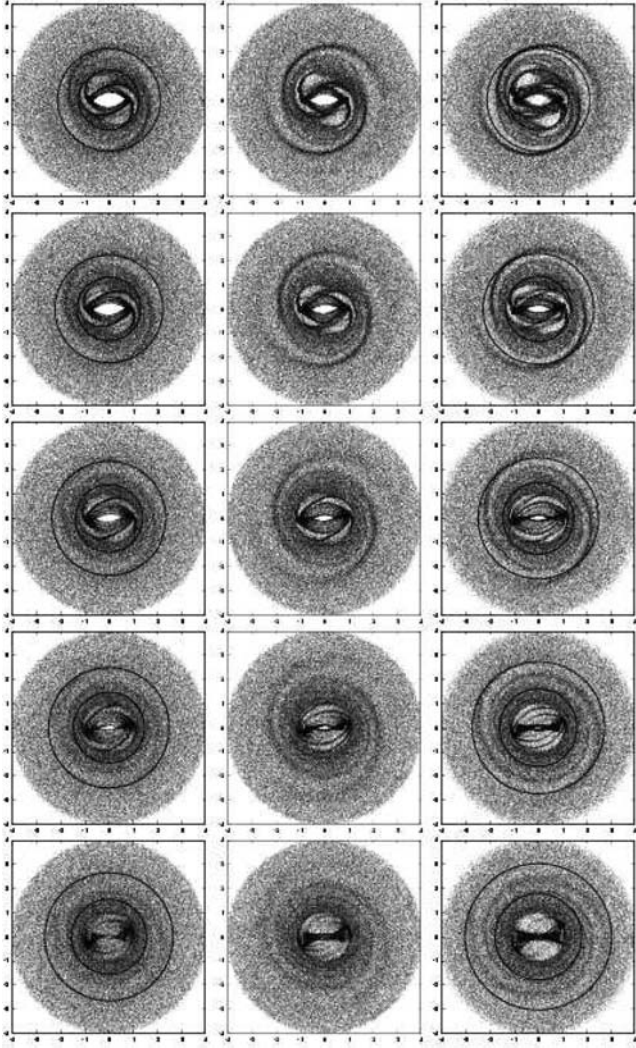


**Figure 11.** Morphology change when the pattern speed is decreased during bar growth. Three frames, corresponding to the last period of bar growth, of the simulations in which the pattern speed is decreased during bar growth. From top to bottom: the rows show simulation 1 with  $d\Omega_g/dt = 0.0$ ; simulation 16 with  $d\Omega_g/dt = -0.0025$ ; simulation 17 with  $d\Omega_g/dt = -0.005$ ; simulation 18 with  $d\Omega_g/dt = -0.0075$ ; and simulation 19 with  $d\Omega_g/dt = -0.01$ . Solid circles in the first and last images of each row show how the bar's corotation resonance and 2:1 OLR change with the decreasing bar pattern speed. Transient spiral structure during bar growth is weaker when the bar is slowing down.

In Fig. 12, we compare the last period of bar growth of simulation 1 and simulations 20–24.  $|\epsilon_{t\text{grow}}|$  increases from 0.06 (top row of Fig. 12) to 0.16 (bottom row). Strong transient spiral structure forms notably earlier, when the bar is stronger.

By the third period of simulation 24 in the bottom row,  $|\epsilon_{t\text{grow},24}| = 0.16$  ( $Q_T = 0.32$ ), the pseudo-ring structure most closely resembles that of the fourth period of simulation 1,  $|\epsilon_{t\text{grow},1}| = 0.10$ . Simulation 24 exhibits closed R1R2 structure a half period after bar growth, whereas simulation 1's R1R2 structure is not evident until 1.5 periods after bar growth. Thus, a 60 per cent increase in bar strength accelerates pseudo-ring formation such that closed orbit rings are evident 1 bar period earlier.

We now consider the structure at later times as a function of bar strength. Fig. 13 shows the last bar period of each of the same six simulations, simulations 1 and 20–24. The bar strength,

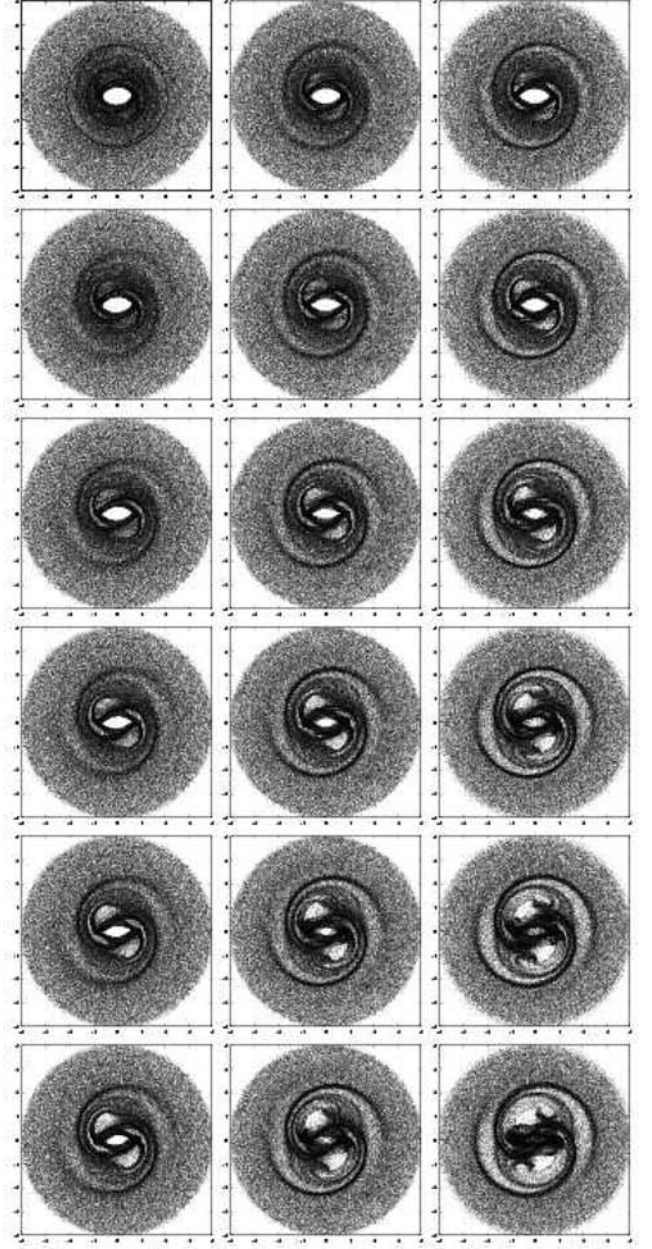


**Figure 12.** Morphology change when the bar strength is altered. Three frames, showing the last period of bar growth, of simulations 1 and 20–24. From top to bottom: the rows show simulation 20 with  $|\epsilon_{t\text{grow}}| = 0.06$ ,  $Q_T = 0.12$ ; simulation 21 with  $|\epsilon_{t\text{grow}}| = 0.08$ ,  $Q_T = 0.16$ ; simulation 1 with  $|\epsilon_{t\text{grow}}| = 0.10$ ,  $Q_T = 0.2$ ; simulation 22 with  $|\epsilon_{t\text{grow}}| = 0.12$ ,  $Q_T = 0.24$ ; simulation 23 with  $|\epsilon_{t\text{grow}}| = 0.14$ ,  $Q_T = 0.28$ ; and simulation 24 with  $|\epsilon_{t\text{grow}}| = 0.16$ ,  $Q_T = 0.32$ . As all of these simulations have the same, unchanging pattern speed,  $\Omega_b = 0.8$ , solid circles showing the bar's corotation resonance and 2:1 OLR are only in the first image of the top row. By the end of the third frame,  $t = t_{\text{grow}}$  and the strength of the bar is equal to the value of the parameter  $|\epsilon_{t\text{grow}}|$ . Bars with higher values of  $|\epsilon_{t\text{grow}}|$ , i.e. stronger bars that grow faster, develop strong spiral structure and outer rings earlier. By the end of the 3 periods of bar growth, our strongest bar (simulation 24,  $|\epsilon_{t\text{grow}}| = 0.16$ ) has pseudo-rings that have almost fully closed to form an R1R2 ring.

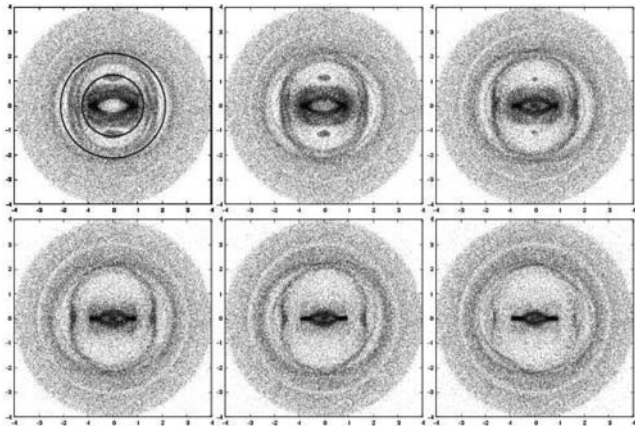


**Figure 13.** The last image of the simulations in which the strength of the bar,  $|\epsilon_{\text{t grow}}|$ , is varied. Each image shows the density distribution at a time 25 bar periods after the start of the simulation. This figure shows the same simulations as Fig. 12. In the first image, solid circles are shown at the location of the bar's corotation resonance and 2:1 OLR, which are the same in each simulation. From left to right: the top row shows simulation 20 with  $|\epsilon_{\text{t grow}}| = 0.06$ ; simulation 21 with  $|\epsilon_{\text{t grow}}| = 0.08$  and simulation 1 with  $|\epsilon_{\text{t grow}}| = 0.10$ . The bottom row shows simulation 22 with  $|\epsilon_{\text{t grow}}| = 0.12$ , simulation 23 with  $|\epsilon_{\text{t grow}}| = 0.14$  and simulation 24 with  $|\epsilon_{\text{t grow}}| = 0.16$ . We find that R1 rings dissolve at later times when the bar strength  $|\epsilon| > 0.15$ .

$|\epsilon_{\text{t grow}}|$ , increases by 0.02 in each successive simulation. In the first and second images, we see a very strong concentration of particles in the R1 ring. By the last image in the second row, however, the R1 ring is almost completely gone. Thus, though the increased bar strength accelerates ring formation at early times, we find that the R1 outer ring dissolves at later times when the bar strength is high, just as it does in Fig. 4 when the pattern speed is increasing after bar growth.

The concentrations of particles above and below the bar that are evident in the weaker bars shown at later times in Fig. 13 are the L4 and L5 Lagrange points and so are corotating with the bar. Small changes in the orbits circulating around these points would cause the particles to circle the bar rather than remain confined to the vicinity of the L4 or L5 point corotating with the bar (e.g. Contopoulos & Patsis 2006). Small variations in pattern speed during or after bar growth (e.g. see Figs 5 and 8) and stronger bars (e.g. Fig. 13) reduce the number of particles near these points. We note that stars and gas are not commonly seen in galaxies at these points, suggesting that weak bars with unchanging pattern speeds and strengths do not persist in galaxies.

## 2.5 Morphology sensitivity to slow variations in bar strength after bar growth

We now consider variations in bar strength after bar growth. In simulations 25–29, we allow the bar strength to grow linearly with time after  $t = t_{\text{grow}}$ . Fig. 14 shows simulation 26 with increasing bar strength. The bar strength at the end of bar growth is  $|\epsilon_{\text{t grow}}| = 0.10$ . It then continues to increase in strength at a slower rate with  $d|\epsilon|/dt = 0.0004$ . The bar strength increases by 3.1 per cent each rotation period reaching a final value of  $|\epsilon| = 0.17$ . As was true for the strong bars of simulations 23 and 24, the R1 ring weakens as the simulation progresses.

Fig. 15 shows the last frame of simulations 1 and 25–29 that have different rates of change in the bar strength following bar growth.

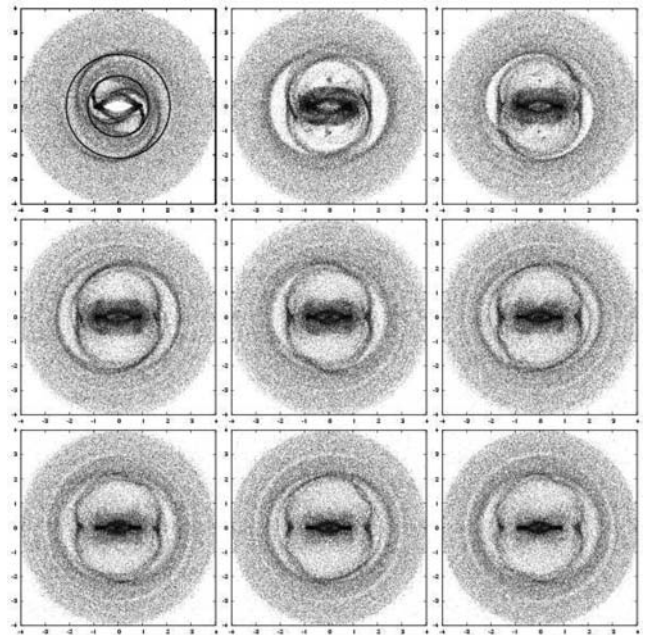


**Figure 14.** Simulation 26 showing a bar with strength increasing after bar growth,  $d|\epsilon|/dt = 0.0004$ . Each image is separated by 2.5 initial bar rotation periods. Solid circles are shown at the location of the bar's corotation resonance and 2:1 OLR at the beginning of the simulation. As was true for the strong bars of simulations 23 and 24, increasing bar strength causes the R1 ring to weaken and dissolve.

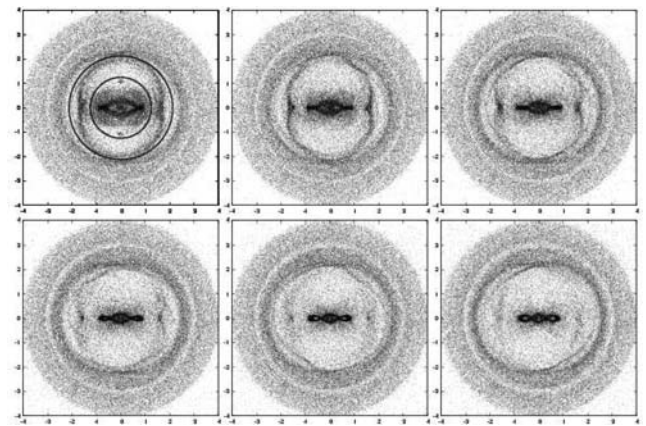


**Figure 15.** The last image of each of the simulations in which bar strength is increasing after  $t = t_{\text{grow}}$ . Each image shows the density distribution at a time 25 bar periods after the start of the simulation. In the first image, solid circles are shown at the location of the bar's corotation resonance and 2:1 OLR, which are the same in each simulation. From left to right: the top row shows simulation 1 with  $d|\epsilon|/dt = 0.0$ ; simulation 25 with  $d|\epsilon|/dt = 0.0002$  and simulation 26 with  $d|\epsilon|/dt = 0.0004$ . The bottom row shows simulation 27 with  $d|\epsilon|/dt = 0.0006$ , simulation 28 with  $d|\epsilon|/dt = 0.0008$  and simulation 29 with  $d|\epsilon|/dt = 0.0010$ . We see the same loss of the R1 ring as that in Fig. 13 (showing the morphology at later times as a function of bar strength) suggesting that bars with  $|\epsilon| \gtrsim 0.16$  cannot maintain stable R1 rings.

We find that by the 25th bar period the density distributions of these simulations exhibit the same loss of the R1 ring as the simulations in which we increased the value of the bar strength  $|\epsilon_{\text{t grow}}|$  (see Fig. 13).

We can conclude that an increase in bar strength dissolves the R1 ring. We lose the R1 ring if the bar becomes 60 per cent stronger

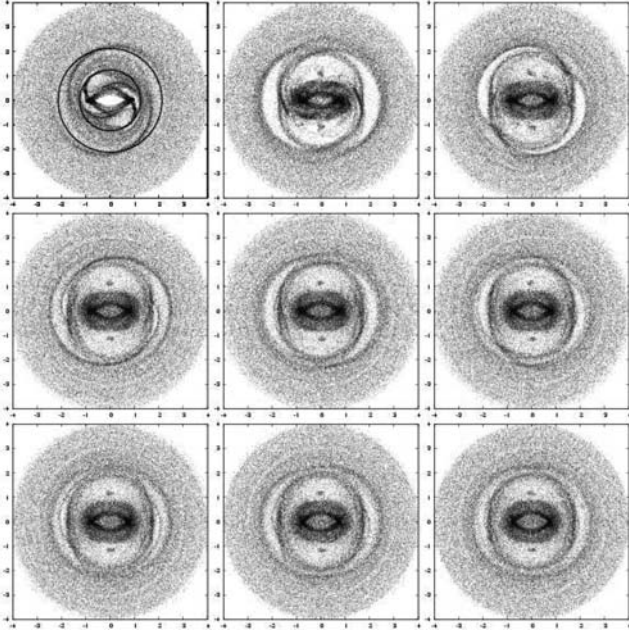


**Figure 16.** Simulation 32 showing a bar with decreasing strength,  $d|\epsilon|/dt = -0.0003$ . The bar strength decreases linearly with time after bar growth is complete. Each image is separated by 2.5 initial bar periods. Solid circles are shown at the location of the bar's corotation resonance and 2:1 OLR at the beginning of the simulation. The R1 and R2 rings become more circular as the bar weakens.

( $|\epsilon_{\text{t grow}}| = 0.16$  as opposed to  $|\epsilon_{\text{t grow}}| = 0.10$ ). Simulation 28, which has a bar that increases in strength from  $|\epsilon| = 0.10$  to  $|\epsilon| = 0.24$ , shows a loss of the R1 ring at late times. We therefore find that we also lose the R1 ring if the bar strength increases by  $\sim 140$  per cent compared to its initial value. It does not appear to matter whether this increase in bar strength occurs during bar growth or more slowly after bar growth is completed; we find that the R1 ring dissolves in both cases. Thus, the R1 ring dissolves for bars with higher strengths.

We now consider simulations 30–34, in which the bar strength decreases after bar growth. Fig. 16 shows simulation 32 with  $d|\epsilon|/dt = -0.0003$ , while Fig. 17 shows the last image of simulations 1 and 30–34.

In Fig. 16, showing a bar that decreases in strength after growth, we see the strong open spiral structure during and immediately following bar growth that is displayed by many of our simulations. The R2 ring is misaligned with the bar for  $\sim 5$  bar periods after bar growth. After the R1 and R2 rings form, they begin to lose their respective alignments (perpendicular and parallel) with the bar in favour of more circular orientations. As shown in Fig. 17, we find that the outer rings become circular at later times when the bar strength is decreased after bar growth. The simulations with the weakest bars at the end of the simulation leave behind two circular rings. NGC 2273, an unusual double outer ring galaxy (Buta & Combes 1996), may be an example of a bar that has weakened.

## 2.6 Morphology sensitivity to the ratio of bar corotation radius to bar length

Finally, we explore the effect of altering the ratio of bar CR to bar length. Rautiainen et al. (2008) find that late galaxies have larger bar corotation to bar length ratios,  $(R)$ , and weaker bars. Athanassoula (1992) and Rautiainen et al. (2008) find that  $(R) = 1.1$ – $1.43$  for

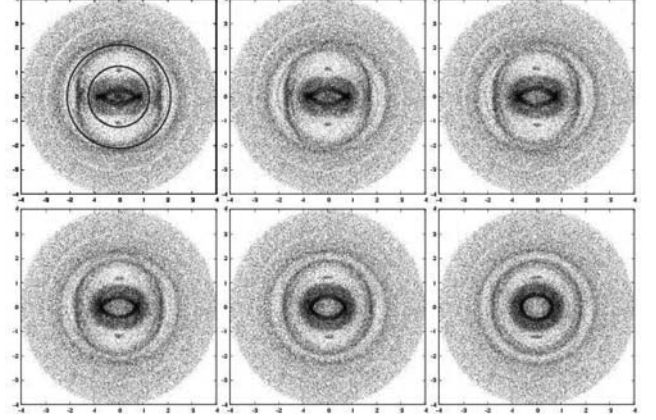


**Figure 17.** The last image of each of the simulations in which the bar is decreasing in strength after growth. Each image shows the density distribution at a time 25 bar periods after the start of the simulation. In the first image, solid circles are shown at the location of the bar's corotation resonance and 2:1 OLR, which are the same in each simulation. From left to right: the top row shows simulation 1 with  $d|\epsilon|/dt = 0.0$ ; simulation 30 with  $d|\epsilon|/dt = -0.0001$  and simulation 31 with  $d|\epsilon|/dt = -0.0002$ . The bottom row shows simulation 32 with  $d|\epsilon|/dt = -0.0003$ , simulation 33 with  $d|\epsilon|/dt = -0.0004$  and simulation 34 with  $d|\epsilon|/dt = -0.0005$ . As the bar becomes weaker the rings separate and become more circular. Two circular rings are left at the end of the simulations that have the weakest bars after 25 bar periods. NGC 2273 with an unusual double outer ring (Buta & Combes 1996) may be an example of a galaxy with a bar that has weakened.

most galaxies. Previously, we have only investigated simulations with an initial bar pattern speed of  $\Omega_{b,0} = 0.8$ , a CR of  $r_{\text{CR}} = 1.25$  and a ratio of bar CR to bar length of  $(R) = 1.25$ . Fig. 18 shows simulation 35 with an initial bar pattern speed of  $\Omega_{b,0} = 0.7$ . The CR here is  $r_{\text{CR}} = 1.43$  and the ratio of CR to bar length is  $(R) = 1.43$ . Fig. 19 shows simulation 36 with an initial bar pattern speed of  $\Omega_{b,0} = 0.9$ , and  $(R) = 1.1$ . Both of these figures may be compared with simulation 1 shown in Fig. 3, for which  $\Omega_{b,0} = 0.8$ ,  $r_{\text{CR}} = 1.25$  and  $(R) = 1.25$ .

In Fig. 18, we note that the spiral-like structure at the end of bar growth is not as strong here as it is in Figs 3 and 19. As was true for the simulations with decreasing bar pattern speed following bar growth (see Fig. 11), transient spiral structure during bar growth is weaker at slower pattern speeds. R1 and R2 rings are present 1 to 2 periods later than in Fig. 3 and 2 to 3 periods later than in Fig. 19. Azimuthal variations in density in the rings and shifts in the R2 ring orientation are present for up to 6 bar periods following bar growth, whereas they are present for only 5 periods in Fig. 3. In Fig. 19, these variations are only present up to the fourth bar period following bar growth, and the R2 ring is oriented parallel to the bar at this point. The time-scale for R2 orientation changes is likely to depend on the libration time-scale in the OLR. When the pattern speed is decreased with respect to the bar length, the OLR is further from the end of the bar and so is likely to have a longer libration time-scale accounting for the increase in the length of time of R2 ring misalignment seen in simulation 35 (shown in Fig. 18).

The rings of Fig. 18 have notably larger radii than the rings of Fig. 19. The radii of the rings shrinks as the CR and the radii of the Lindblad resonances is decreased. Finally, there is a large concentration of particles in the L4 and L5 Lagrange points in Fig. 18, while Fig. 3 shows only a small concentration of particles corotating with the bar at the L4 and L5 points. Fig. 19 shows no such concentrations in the Lagrange points. As mentioned previously, an

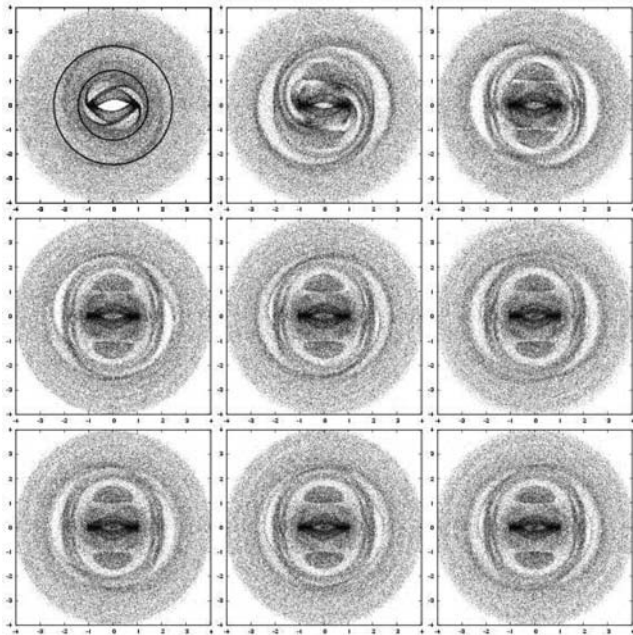


**Figure 18.** Simulation 35 with a slower initial pattern speed of  $\Omega_{b,0} = 0.7$ . The ratio of bar CR to bar length is  $(R) = 1.43$ . Images are separated by 2.5 initial bar rotation periods. In the first image, solid circles are shown at the location of the bar's corotation resonance and 2:1 OLR. A larger ratio of bar CR to bar length results in weaker spiral structure during bar growth. The R2 ring takes longer to become aligned with the bar, and the radii of the rings are larger as the resonances have moved outwards.

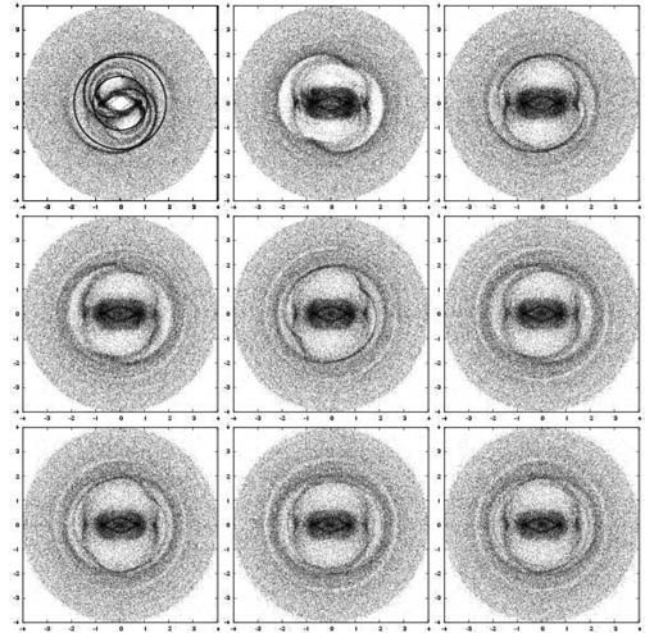


**Figure 19.** Simulation 36 with an initial pattern speed of  $\Omega_{b,0} = 0.9$  and  $(R) = 1.1$ . Images are separated by 2.5 initial bar rotation periods. In the first image, solid circles are shown at the location of the bar's corotation resonance and 2:1 OLR. We see stronger spiral structure during bar growth, and the R1 and R2 rings form and align (perpendicular and parallel, respectively) with the bar earlier than in simulations with slower pattern speeds. The resonances have moved inwards, creating rings with smaller radii.

increase in pattern speed and variations in bar strength will reduce the number of particles that are confined to these points.

### 3 COMPARISON TO RING GALAXY MORPHOLOGY

#### 3.1 Sample

Following the lead of Rautiainen et al. (2008), we compare our simulations to *B*-band galactic images from OSUBSGS. We initially considered all galaxies in the OSUBSGS that are classified as ring galaxies; however, we then restricted our choices of galaxies to those that have clearly visible outer rings in the *B*-band images and with inclinations below  $60^\circ$ , so that they could be compared to the morphology of our simulations. We also restricted our comparison galaxies to early-type barred spiral galaxies as they contain less gas and dust compared to later type galaxies and so would be more appropriately compared to our collisionless dissipationless simulations. We include two additional galaxies, NGC 4314 and 4548, that are not classified as ring galaxies, but have strong bars and display R1'-type ring morphology. Our sample of comparison objects consists of nine spiral galaxies with morphological classifications ranging from SB0/a to SBbc. These classifications are based on those put forth by de Vaucouleurs, de Vaucouleurs & Corwin (1976). One of the galaxies is weakly barred, NGC 4457, with maximum  $Q_T \sim 0.1$  (Laurikainen et al. 2004). The galaxies that we compare to our simulations are listed in Table 3 with Hubble type, inclination with respect to the line of sight, ratio of bar CR to bar length, distance, *H*-band magnitude from the Two-Micron All-Sky Survey (2MASS) extended source catalogue, estimated circular velocity, bar length, strength and estimated bar rotation periods. The

ratios of bar CR to bar length,  $(R)$ , are taken from Rautiainen, Salo & Laurikainen (2005). Bar lengths and strengths ( $Q_T$ ) are taken from the measurements by Laurikainen et al. (2004). Distances in Mpc are from the HYPERLEDA data base (Paturel et al. 2003) calculated using velocities corrected for infall of the Local Group towards Virgo and a Hubble constant  $H_0 = 70 \text{ km s}^{-1} \text{ Mpc}^{-1}$ . Inclinations are those from the HYPERLEDA data base (Paturel et al. 2003). The circular velocity is estimated from the *H*-band magnitude and the luminosity linewidth relation by Pierce & Tully (1992).

For each galaxy in our comparison sample, we ran simulations with bar strengths that matched those measured by Laurikainen et al. (2004) and pattern speeds matching those estimated by Rautiainen et al. (2005), though we note that Rautiainen et al. (2005) used a gravitational potential estimated from *H*-band images and our study assumes a flat rotation curve and a simplified bar model. When comparing galaxies to our simulations, we focus on the location, orientation and morphology of the spiral arms and outer rings. We searched through our bank of simulations for images that best resembled the outer ring galaxy morphology. Galaxy images have been corrected for inclination and rotated so that the bar lies horizontal in our figures. In some cases, the galaxy images have been flipped so that the galaxy is rotating counter clockwise and so is in the same direction as our simulations. We do not include solid circles at the locations of the bar's corotation resonance and 2:1 OLR in our simulations. We found that these circles often obstruct the structure crucial for our comparisons.

We first compare galaxies with strong R1' pseudo-ring morphology to morphology displayed by our simulations during bar growth. We then focus on galaxies with R1R2 rings. Finally, we explore simulations that can account for the weak bar and distant outer ring present in NGC 4457.

**Table 3.** Ring galaxy estimated bar rotation periods.

	Type	$i$	$Q_T$	$(R)$	$D$ (Mpc)	$m_H$ (mag)	$m_H$ (mag)	$v_c$ (km s <sup>-1</sup> )	$r_b$ (kpc)	$P_b$ (Myr)
	1	2	3	4	5	6	7	8	9	10
NGC 1300	(R')SB(s)bc	49.3	0.54		20.1	7.770	-23.7	258.6	8.5	206.7
NGC 3504	(R)SAB(s)ab	53.4	0.29	1.14	23.9	8.609	-23.3	234.7	7.0	187.6
NGC 4314	SB(rs)a	16.2	0.44	1.07	16.4	7.725	-23.3	234.7	6.0	160.7
NGC 4457	(R)SAB(s)0/a	34.6	0.09	0.89	13.4	8.015	-22.6	198.1	2.9	92.0
NGC 4548	SB(rs)b	37.0	0.34	1.32	8.5	7.373	-22.3	184.2	2.8	95.5
NGC 5101	(R)SB(rs)0/a	23.2	0.19		25.2	7.401	-24.6	321.7	8.5	166.2
NGC 5701	(R)SB(rs)0/a	41.3	0.14	1.19	22.9	8.358	-23.4	240.5	5.5	143.8
NGC 6782	(R')SB(r)0/a	56.0	0.17	1.18	52.0	9.115	-24.5	314.0	11.7	234.4
NGC 7552	(R')SB(s)ab	23.6	0.40	0.97	20.1	7.840	-23.7	258.6	6.8	165.3

*Note.* Column (1): morphological classifications by de Vaucouleurs et al. (1976), except those for NGC 1300 and 6782, which are by de Vaucouleurs et al. (1991). Column (2): inclinations from the HYPERLEDA data base (Paturel et al. 2003). Column (3): maximum gravitational bar torque per unit mass per unit square of the circular speed measured by Laurikainen et al. (2004). Column (4): ratio of bar CR to bar length estimated by Rautiainen et al. (2005). ( $R$ ) = 1.25 was used for the comparison simulations of NGC 1300 and 5101.) Column (5): distances in Mpc from the HYPERLEDA data base (Paturel et al. 2003) calculated using velocities corrected for infall of the Local Group towards Virgo and a Hubble constant  $H_0 = 70 \text{ km s}^{-1} \text{ Mpc}^{-1}$ . Column (6): total integrated flux magnitudes in  $H$  band from the 2MASS-extended source catalogue (Jarrett et al. 2000). Column (7): absolute magnitudes in the  $H$  band. Column (8): circular velocities estimated from the  $H$ -band magnitude using the luminosity linewidths relation by Pierce & Tully (1992). Column (9): bar lengths measured by Laurikainen et al. (2004). In their paper, Laurikainen et al. (2004) define the bar length to be the radius of the bar region at which the phases of the  $m = 2$  and 4 density amplitudes are constant. Column (10): periods of bar rotation calculated using the angular frequencies defined by  $\Omega = v_c/r_b$ .

### 3.2 Comparison of particle simulations to galaxies exhibiting similar spiral-like structure

Fig. 20 shows four galaxies, with strong R1'-type pseudo-rings: NGC 4548, 7552, 1300 and 4314. We find that our simulations reasonably match the morphologies of the galaxies when they are run with the pattern speed estimates of Rautiainen et al. (2005). Thus the simulations have  $\Omega_{b,0} = 0.758$  ( $(R) = 1.32$ ) for NGC 4548,  $\Omega_{b,0} = 1.03$  ( $(R) = 0.97$ ) for NGC 7552 and  $\Omega_{b,0} = 0.935$  ( $(R) = 1.07$ ) for NGC 4314. Rautiainen et al. (2005) does not present a pattern speed estimate for NGC 1300. We have compared NGC 1300 with a simulation with  $\Omega_{b,0} = 0.8$  ( $(R) = 1.25$ ) as this falls in the range presented by Rautiainen et al. (2008), ( $R$ ) = 1.1–1.43. In each simulation, the bar grows for 3 initial bar periods.

Each of the galaxy images is compared with the density distribution at a time during or just following bar growth. NGC 4548 and 7552 have the weakest strengths  $Q_T = 0.34$  and  $0.4$  ( $|\epsilon_{\text{tgrw}}| = 0.17$  and  $0.20$ ), respectively. NGC 4314 and 1300 have stronger bars with  $Q_T = 0.44$  and  $0.54$  ( $|\epsilon_{\text{tgrw}}| = 0.27$  and  $0.22$ ), respectively. The simulations show stronger spiral structure at late times during bar growth and for stronger bars. Transient spiral structure during bar growth is also stronger for faster pattern speeds. NGC 4548, which has weaker spiral structure when compared to the other galaxies, has both the weakest and the slowest bar. The simulation matching NGC 4548 is shown at a time 1.5 bar periods from the beginning of the simulation. Snapshots of the simulations for the other galaxies are given at  $t = 2P_{b,0}$ ,  $2.5P_{b,0}$  and  $3P_{b,0}$  for NGC 7552, 1300 and 4314, respectively (for  $P_{b,0}$  initial bar rotation periods). NGC 7552 has a stronger bar than NGC 4548 resulting in stronger spiral structure during bar growth. NGC 1300 has the strongest spiral structure but also has the strongest bar. NGC 4314's spiral structure is not as narrow as for the other galaxies. We find a better match of morphologies between NGC 4314 and our simulation when we increase the initial velocity dispersion of our simulation from 0.04 to 0.07. The outer disc of NGC 4314 is devoid of star formation suggest-

ing that an initial velocity dispersion typical of a stellar disc rather than a gaseous one should be used. The increase in velocity dispersion decreases the strength of the arms displayed by the simulation, requiring a later time to match the observed morphology.

We find that our simulations display reasonable matches to observed R1' ring morphology near the end of bar growth when strong spiral pseudo-rings are displayed by our simulations. It is likely that these galaxies have experienced recent bar growth. These bars could still be growing. We note that R1' pseudo-ring structure is displayed for a longer time-scale (up to a few bar rotation periods following bar growth) by SPH and sticky-particle simulations (Byrd et al. 1994; Ann & Lee 2000). This comparison suggests that our dissipationless simulations could underestimate the longevity of R1' structure.

### 3.3 R1R2 rings

We now compare our simulations to galaxies that display R1R2 morphology which is exhibited by our simulations following bar growth. We begin by comparing our simulations to two galaxies that exhibit R1R2' morphology. Depending on the strength of the bar, the R2 ring can remain misaligned with the bar for up to  $\sim 10$  bar periods following growth. Fig. 21 shows R1R2' galaxies that exhibit structure similar to that in our simulations that is evident before the R2 ring aligns with the bar. From top to bottom, Fig. 21 shows NGC 5701 and 5101.

Fig. 22 compares NGC 6782 and 3504 with density distributions showing simulations that have stabilized and exhibit R1R2 morphology.

NGC 5701 is a fairly weak bar with  $Q_T = 0.14$  that shows a strong R1 ring but a weaker R2 ring. NGC 5701 is compared to a simulation with  $\Omega_{b,0} = 0.84$  ( $(R) = 1.19$ ) one period after bar growth has completed. At this time, the spiral arms generated during bar growth are beginning to close and will soon form both R1 and R2 rings. As NGC 5701 has a weaker bar, it may take longer



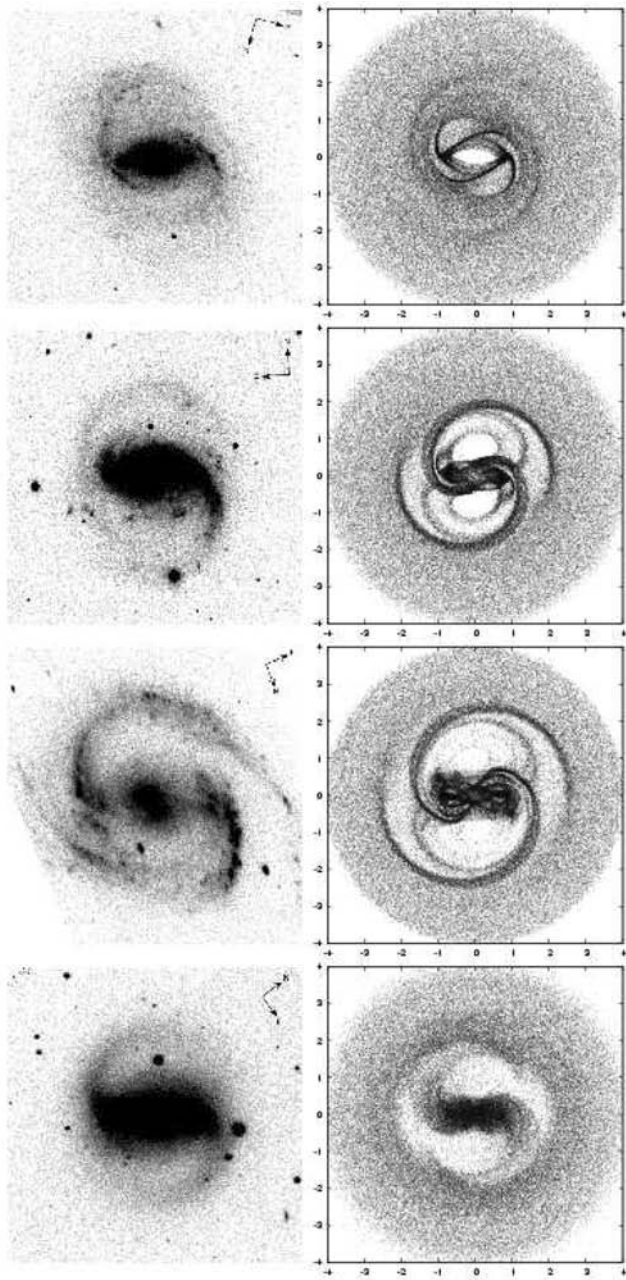


**Figure 20.** We compare the pseudo-rings of four galaxies with the structure created during bar growth in our simulations. From top to bottom: row 1 shows NGC 4548 compared with a simulation with  $|\epsilon_{\text{tgrw}}| = 0.17$  and  $\Omega_{b,0} = 0.76$ ; row 2 shows NGC 7552 with  $|\epsilon_{\text{tgrw}}| = 0.20$  and  $\Omega_{b,0} = 1.03$ ; row 3 shows NGC 1300 with  $|\epsilon_{\text{tgrw}}| = 0.27$  and  $\Omega_{b,0} = 0.8$  and row 4 shows NGC 4314 with  $|\epsilon_{\text{tgrw}}| = 0.22$  and  $\Omega_{b,0} = 0.94$ . Galaxy images are on the left-hand side and simulations on the right-hand side. Galaxy images have been corrected for inclination and rotated so that the bar lies horizontal. For some galaxies, the galaxy image has been inverted so that the galaxy is viewed rotating counter clockwise. The simulation for NGC 4548 is shown at  $t = 1.5P_{b,0}$ , (for  $P_{b,0}$  initial bar rotation periods) from the beginning of the simulation. That for 7552 is shown at  $t = 2P_{b,0}$ , that for NGC 1300 at  $t = 2.5P_{b,0}$  and that for NGC 4314 at  $3P_{b,0}$ . The simulations for NGCs 4548, 7552 and 1300 are shown during bar growth, and that for NGC 4314 right at the end of bar growth. The initial orbits for the NGC 4314 simulation had twice the velocity dispersion of the other simulations.

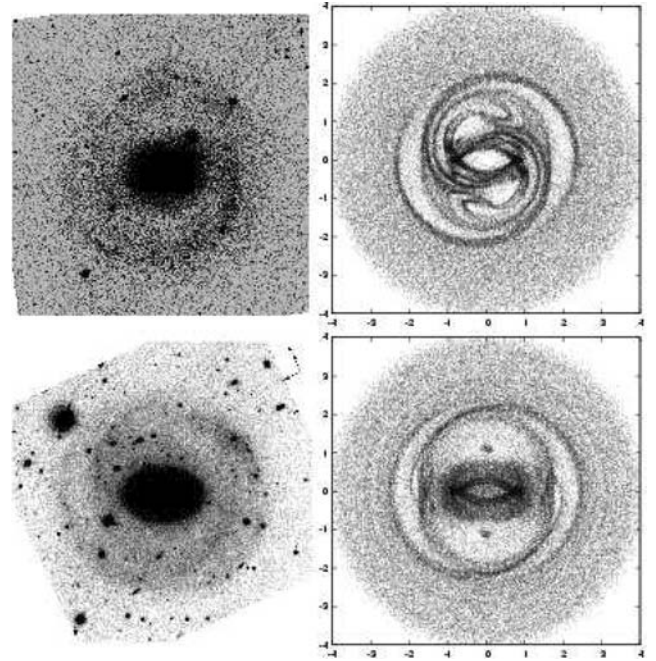


**Figure 21.** The top row shows NGC 5701,  $Q_T = 0.14$ , compared with the fourth period of a simulation with a bar strength of  $|\epsilon_{\text{tgrw}}| = 0.07$  and a bar pattern speed of  $\Omega_{b,0} = 0.84$ . This is 1 period after bar formation is complete. The bottom row shows NGC 5101,  $Q_T = 0.19$ , compared with the density distribution of a simulation with a bar strength of  $|\epsilon_{\text{tgrw}}| = 0.095$  and a bar pattern speed of  $\Omega_{b,0} = 0.8$  7.5 periods after bar growth. The ring structure of these galaxies is similar to the broken or misaligned rings shown in our simulations a few rotation periods following bar growth.

for R1 and R2 rings to form and become aligned perpendicular and parallel with the bar, respectively.

NGC 5101 is somewhat stronger with  $Q_T = 0.19$ , and displays both R1 and R2 rings. It is compared to a simulation with  $\Omega_{b,0} = 0.8$  ( $(R) = 1.25$ ) 7.5 periods following bar growth. (As with NGC 1300,  $\Omega_{b,0} = 0.8$  was used because Rautiainen et al. (2005) do not have a pattern speed estimate for NGC 5101.) The R2 ring at this time is misaligned with the bar similar to the misalignment in the galaxy. The galaxy displays a more elliptical ring than that of our simulation. A number of factors could account for this discrepancy. The bar could be slowing down and causing increased epicyclic motion in the R2 ring due to resonance capture. We may not have corrected for inclination correctly, or the rotation curve could be dropping in this region, causing the OLR to be stronger than we have considered here with a flat rotation curve.

The simulations we have chosen to match the galaxies with R1R2 morphology have bars with fixed pattern speeds. Reasonable matches between observed and simulated morphology are found a few periods following bar growth during which time our simulations contain both R1 and R2 rings but still exhibit asymmetries in the R2 ring. Based on the exploration in Section 2.2, we can conclude that the bars in these galaxies are unlikely to have increased in pattern speed as this would have destroyed the R1 ring. Moderate decreases in bar pattern speed could have occurred.

We now compare our simulations to two galaxies that exhibit R1R2 morphology. In Fig. 22, NGC 6782 is compared to the fifth period (2 periods after bar growth is complete) of a simulation with a bar pattern speed of  $\Omega_{b,0} = 0.847$  and a bar strength of  $|\epsilon_{\text{tgrw}}| = 0.085$ . NGC 3504 is compared to a simulation with  $\Omega_{b,0} = 0.877$  and  $|\epsilon_{\text{tgrw}}| = 0.145$  one half bar period after bar growth.



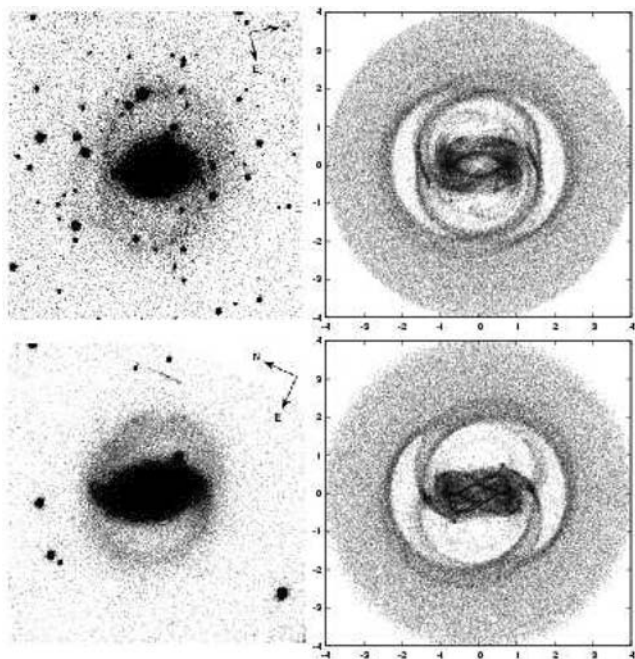


**Figure 22.** We compare NGC 6782 and 3504 to density distributions of simulations after bar growth. The top row compares NGC 6782,  $Q_T = 0.17$ , to the second period following bar growth of a simulation with a bar of strength  $|\epsilon_{\text{tgrw}}| = 0.085$  and bar pattern speed of  $\Omega_{b,0} = 0.847$ . The bottom row shows NGC 3504,  $Q_T = 0.29$ , compared to a simulation with  $|\epsilon_{\text{tgrw}}| = 0.145$  and bar pattern speed of  $\Omega_{b,0} = 0.877$  one half period after bar growth. The bars of these galaxies may be responsible for the R1 structure visible in these images. The galaxies' R2 rings may be present but not visible in the  $B$  band.

NGC 6782 has a bar with  $Q_T = 0.17$ . Because of the weaker bar, the R2 ring in NGC 6782's comparison simulation remains misaligned with the bar for  $\sim 6$  bar periods following bar growth. The spiral-like structure evident during bar growth does not close to form R1 and R2 rings until 2 periods after bar growth, in the snapshot shown in Fig. 22. There is a reasonable match between the R1 structure of NGC 6782 and that exhibited by our simulation.

For NGC 3504  $Q_T = 0.29$ , a much stronger bar than NGC 6782. R1 and R2 rings are evident only 1 period after bar growth, and the R2 ring is aligned with the bar within 4 bar rotation periods following bar growth. As with NGC 4314 in Fig. 21, the strong bar leads to a weakening of the R1 ring.

Sticky particles simulations by Schwarz (1984) displayed R1 or R2 morphology depending on the initial gas distribution. Either dissipation is required to exhibit R1 morphology only, or the initial stellar and gas distribution is different for the galaxies showing longer lived R1 morphology.

### 3.4 Dissolving the R1 ring and NGC 4457

We found in Section 2.2 that the R1 ring dissolves when the bar pattern speed increases by more than  $\sim 8$  per cent after bar growth. We see the same loss of the R1 ring if the bar has strength  $|\epsilon_{\text{tgrw}}| > 1.5$  or if the bar strength increases by  $\gtrsim 140$  per cent after bar growth. In either case, the R1 ring is destroyed leaving a nearly circular R2 ring.

NGC 4457, an (r)SAB(s)0/a galaxy, appears to be lacking an R1 ring. According to Laurikainen et al. (2004), NGC 4457's bar has  $Q_T = 0.09$ , which corresponds to a very weak bar. It is therefore

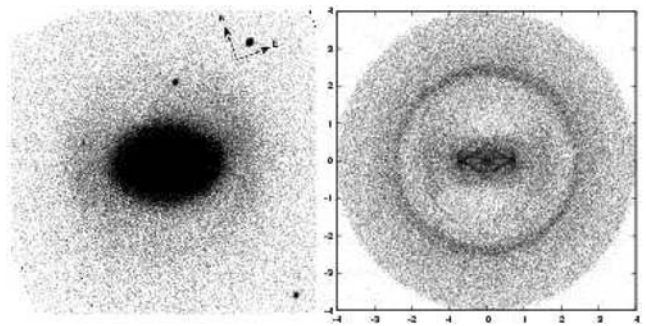


**Figure 23.** NGC 4457 compared to the 25th frame of simulation 5, which has a bar with increasing pattern speed;  $d\Omega_b/dt = 0.0004$ . Both the galaxy and the simulation lack an R1 outer ring but do maintain a nearly circular outer ring. [The bar strength measured by Laurikainen et al. (2004) is too weak to destroy the R1 ring, and the galaxy is not compared with a simulation with bar pattern speed measured by Rautiainen et al. (2005) because we find that a loss of R1 ring is caused by the pattern speed increasing after bar growth.]

unlikely that loss of the R1 ring is due to the strength of the bar, as we find that strong bars dissolve the R1 ring and weakening bars can leave behind a double ring. It is possible, however, that the lack of an R1 ring is the result of a bar that has increased in pattern speed. Rautiainen et al. (2005) find that  $\langle R \rangle = 0.89$  for NGC 4457 corresponding to a bar pattern speed of  $\Omega_b = 1.12$ . However, our simulations with this pattern speed exhibit an R1 ring along with a circular R2 ring. It is possible that the bar pattern speed of NGC 4457 was increasing after bar growth and that the R1 ring was subsequently destroyed. For this reason, in Fig. 23 we do not use a simulation with the pattern speed estimate of Rautiainen et al. (2005) for comparison. Instead, NGC 4457 is compared with the 25th period of simulation 5, which has a bar that is speeding up after bar growth,  $d\Omega_b/dt = 0.0004$ . NGC 4457's outer rings are very faint in the  $B$ -band image, yet it does appear that the outer ring is circular and no R1 ring is evident. It is possible that the pattern speed of this galaxy's bar has increased since the bar finished growing, thereby destroying any R1 ring that would have formed shortly after bar growth.

## 4 DISCUSSION AND SUMMARY

We have presented integrations of collisionless massless particles perturbed by growing and secularly evolving bar perturbations. We find that collisionless simulations can exhibit double-ringed R1 and R2 outer ring morphology with rings both perpendicular (R1) and parallel (R2) to the bar. In the last period of bar growth, strong open spiral structure is exhibited resembling an R1' pseudo-ring. For 2–3 periods following bar growth, R1 and R2 rings are seen with the R2 ring changing in orientation and azimuthal density contrast. Thus, R1R2' pseudo-ring morphology is displayed within a few bar periods following bar growth. Our simulations start with particles in nearly circular orbits with velocity dispersions equivalent to  $7 \text{ km s}^{-1}$  for a  $200 \text{ km s}^{-1}$  rotation curve. This suggests sticky-particle simulations have been successful in exhibiting R1R2 ring morphology because the velocity dispersion of orbits is damped and so particles are in initially nearly circular orbits.

In our collisionless simulations, we find that the outer rings with major axis perpendicular (R1) to the bar are fragile. If the bar pattern speed increases more than 8 per cent after bar growth, or if the bar strength is higher than or increases past  $|\epsilon| \gtrsim 0.16$  or  $Q_T \gtrsim 0.32$ , the R1 outer ring will dissolve after  $\sim 20$  bar periods. The simulations

are then nearly mirror symmetric and do not display asymmetries typical of pseudo-rings.

Stronger bars can form R1' pseudo-rings earlier. However, if the bar strength is  $|\epsilon| \gtrsim 0.16$  or  $Q_T \gtrsim 0.32$  the R1 ring will dissolve after  $\sim 20$  bar rotation periods. If the bar strength increases to this value subsequent to formation, the R1 ring also dissolves.

We find that a decrease in the bar pattern speed after bar growth causes particles to be captured in orbits parallel to the bar which are increased in epicyclic amplitude as the bar slows down. Strong R1 and elongated R2 rings persist in these simulations. Misalignments between the R2 ring and the bar also persist so the galaxy can exhibit R1R2' pseudo-ring morphology for a longer period of time. If the bar pattern speed slows down more than  $\sim 3.5$  per cent, the R2 ring develops a scallop above and below the bar. As these are not observed in galaxies, bars probably do not slow down more than  $\sim 3.5$  per cent without also varying in strength.

Sandage & Bedke (1994) find that early-type barred galaxies often have semi-detached outer rings (e.g. NGC 1543; Buta & Combes 1996 and NGC 4457). These galaxies may contain bars that have increased in pattern speed or were once strong and so destroyed their R1 ring. If the bar weakens, the R1 and R2 rings can be left behind as two nearly circular rings, similar to those observed in the unusual double outer ringed galaxy NGC 2273.

We find that the morphology of our simulations resembles that of R1' ringed galaxies if the simulation time is chosen during or just after bar formation. We find we can match pseudo-ring morphology with simulations that have bar strengths estimated from the bar shapes. Stronger and longer spiral arms are seen later in the simulation and in more strongly barred systems. The constraint on simulation time-scale suggests that R1' ring morphology is a sign-post of recent bar formation. We note that sticky particle and SPH simulations exhibit R1 pseudo-ring morphology a few bar rotation periods longer than ours suggesting that the dissipationless simulations explored here underestimate the longevity of these features.

We find that galaxies with R1R2' morphology are well matched by simulations a few bar rotation periods following bar growth. As R1 rings are fragile, we infer that these galaxies have had stable bars that have not experienced large changes in either pattern speed or strength.

The exploration of parameter space in the collisionless dissipationless limit done here can be used by future work to differentiate between phenomena that would be exhibited by collisionless models and that is a result of dissipation. A better understanding of the role of dissipation in affecting outer ring morphology should allow observationally based constraints on the secular evolution of bars.

Only 10–20 per cent of early-type galaxies exhibit outer rings with pseudo-rings being more prevalent in later type galaxies (Buta & Combes 1996). Not all but most galaxies classified with outer rings are barred suggesting that only 15–40 per cent of barred galaxies exhibit outer rings. Here, we have found that R1' and R1R2' galaxies are likely to represent different times since bar formation with R1' galaxies representing an earlier time-scale during or just after bar formation and R1R2 morphology representing galaxies with stable bars a few bar rotation periods following bar formation. Galaxies in these two transient categories probably comprise a significant fraction of all outer ring galaxies. This suggests that most outer ring galaxies represent morphology that is only present for a few bar rotation periods. It is interesting to ask what time-scales these morphologies correspond to. Bar rotation periods for the ringed galaxies in our sample range from  $\sim 100$  to 200 Myr (see Table 3). The R1' classification may only last a few bar rotations or 0.5 Gyr and the R1R2' classification only  $\sim 1$  Gyr. Both of these

time-scales are short compared to the lifetime of a galaxy. Ringed galaxies lacking R1 rings may be longer lived but may provide evidence for bar evolution. It is likely that only a low fraction of barred galaxies might be considered systems that are not evolving secularly or have not formed in the last Gyr.

## ACKNOWLEDGMENTS

We thank Eija Laurikainen for helpful correspondence. This work made use of data from the OSUBSGS, which was funded by grants AST-9217716 and AST-9617006 from the United States National Science Foundation, with additional support from the Ohio State University. This project was supported in part by NSF award PHY-0552695. We acknowledge the usage of the HYPERLEDA data base (<http://leda.univ-lyon1.fr>). This publication makes use of data products from the 2MASS, which is a joint project of the University of Massachusetts and the Infrared Processing and Analysis Center/California Institute of Technology, funded by the National Aeronautics and Space Administration and the National Science Foundation.

## REFERENCES

- Ann H. B., Lee H. M., 2000, JKAS, 33, 1
- Athanassoula E., 1992, MNRAS, 259, 345
- Athanassoula E., 2003, MNRAS, 341, 1179
- Bissantz N., Englmaier P., Gerhard O., 2003, MNRAS, 340, 949
- Bournaud F., Combes F., 2002, A&A, 392, 83
- Buta R., Combes F., 1996, Fundam. Cosm. Phys., 17, 95
- Byrd G., Rautiainen P., Salo H., Buta R., Crocker D. A. 1994, AJ, 108, 476
- Combes F., Gerin M., 1985, A&A, 150, 327
- Combes F., Sanders R. H., 1981, A&A, 96, 164
- Contopoulos G., Grosbøl P., 1989, Astron. Astrophys. Rev., 1, 261
- Contopoulos G., Patsis P. A., 2006, MNRAS, 369, 1054
- Das M., Teuben P. J., Vogel S. N., Regan M. W., Sheth K., Harris A. I., Jefferys W. H., 2003, ApJ, 582, 190
- Debattista V. P., Sellwood J. A., 1998, ApJ, 493, L5
- Dehnen W., 2000, AJ, 119, 800
- de Vaucouleurs G., de Vaucouleurs A., Corwin H. G., 1976, Second Reference Catalogue of Bright Galaxies. University of Texas Press, Austin
- de Vaucouleurs G., de Vaucouleurs A., Corwin H. G., Jr, Buta R., Paturel G., Fouque P., 1991, Third Reference Catalogue of Bright Galaxies. Springer-Verlag, New York
- Eskridge P. B. et al., 2002, ApJS, 143, 73
- Hänninen J., Salo H., 1992, Icarus, 97, 228
- Hunter J. H., Jr, England M. N., Gottesman S. T., Ball R., Huntley J. M., 1988, ApJ, 324, 721
- Jarrett T. H., Chester T., Cutri R., Schneider S., Skrutskie M., Huchra J. P., 2000, AJ, 119, 298
- Kalnajs A. J., 1991, in Sundelius B., ed., Dynamics of Disc Galaxies. Göteborg, Sweden, p. 323
- Laurikainen E., Salo H., Buta R., Vasylyev S., 2004, MNRAS, 355, 1251
- Lindblad P. A. B., Lindblad P. O., Athanassoula E., 1996, A&A, 313, 65
- Martinez-Valpuesta I., Shlosman I., Heller C., 2006, ApJ, 637, 214
- Minchev I., Nordhaus J., Quillen A. C., 2007, ApJ, 664, L31
- Paturel G., Petit C., Prugniel P., Theureau G., Rousseau J., Brouty M., Dubois P., Cambrésy L., 2003, A&A, 412, 45
- Pierce M. J., Tully R. B., 1992, ApJ, 387, 47
- Quillen A. C., 2003, AJ, 125, 785
- Quillen A., 2006, MNRAS, 365, 1367
- Rautiainen P., Salo H., 2000, A&A, 362, 465
- Rautiainen P., Salo H., Buta R., 2004, MNRAS, 349, 933
- Rautiainen P., Salo H., Laurikainen E., 2005, ApJ, 631, L129

- Rautiainen P., Salo H., Laurikainen E., 2008, MNRAS, 388, 1803  
Romero-Gomez M., Masdemont J. J., Athanassoula E., Garcia-Gomez C., 2006, A&A, 453, 39  
Salo H., Rautiainen P., Buta R., Purcell G. B., Cobb M. L., Crocker D. A., Laurikainen E., 1999, AJ, 117, 792  
Sandage A., Bedke J., 1994, The Carnegie Atlas of Galaxies. Carnegie Inst. of Wash., Washington D.C.

- Schwarz M. P., 1981, ApJ, 247, 77  
Schwarz M. P., 1984, Proc. Astron. Soc. Aust., 5, 464  
Sellwood J. A., Debattista V. P., 2006, ApJ, 639, 868  
Voglis N., Harsoula M., Contopoulos G., 2007, MNRAS, 381, 757

This paper has been typeset from a  $\text{\LaTeX}$  file prepared by the author.